





# Interaction regimes of a vortex ring and an inertial particle

Guilherme Siqueira de Aquino<sup>1</sup> , Sylvain Viroulet<sup>1</sup> , Nicolas Sasso<sup>1</sup>  and Julie Albagnac<sup>1</sup> 

<sup>1</sup>Univ Toulouse, Toulouse INP, CNRS, IMFT, Toulouse, France

**Corresponding author:** Sylvain Viroulet, [sylvain.viroulet@imft.fr](mailto:sylvain.viroulet@imft.fr)

(Received 23 April 2025; revised 22 September 2025; accepted 3 November 2025)

The interaction between a coherent vortex ring and an inertial particle is studied through a combination of experimental and numerical methods. The vortex ring is chosen as a model flow ubiquitous in various geophysical and industrial flows. A detailed description of the vortex properties together with the evolution of the particle kinematics during the interaction is addressed thanks to time-resolved particle image velocimetry and three-dimensional shadowgraphy visualisations. Complementary, direct numerical simulations are realised with a one-way coupling model for the particle, allowing for the identification of the elementary forces responsible for the interaction behaviours. The experimental and numerical results unequivocally demonstrate the existence of three distinct interaction regimes in the parameter range of the present study: simple deviation, strong deviation and capture. These regimes are delineated as functions of key controlled dimensionless parameters, namely, the Stokes number and the initial radial position of the particle relative to the vortex ring axis of propagation.

**Key words:** vortex interactions, vortex dynamics, particle/fluid flows

## 1. Introduction

Particle-laden flows are ubiquitous in a wide range of natural phenomena, such as plastic transport in the ocean (van Sebille *et al.* 2020), phytoplankton dynamics in migration strategy (Sengupta, Carrara & Stocker 2017), and volcanic plumes produced during volcanic eruptions (Rossi *et al.* 2021). This type of flow is also widely encountered in industrial processes, such as fluidised beds, pneumatic powder conveying and cyclone

separators (e.g. Grimble, Agarwal & Juniper 2017; Neau *et al.* 2020; Grosshans *et al.* 2021).

The interactions between the continuous and dispersed phases are highly dependent on various flow and particle features. On the one hand, particles can be regarded as inertial or passive tracers depending on their response time relative to the characteristic time scale of the surrounding flow. In addition, the particle volume fraction can play a role in their individual or collective kinetics, and may, in return, modify the flow. On the other hand, the flow can also have specific characteristics, such as the presence of sheared or swirling zones. The dynamics of particles in a non-uniform flow swiftly become challenging to predict (see Mathai, Lohse & Sun (2020) and Brandt & Coletti (2022) for a comprehensive review). Despite major progress in modelling such a flow, the understanding, and therefore the control of transport and dispersion of particles, remains limited to canonical configurations. Regarding the fluid transporting the particles, when dealing with turbulent flows involving coherent vortical structures, the interactions are governed by various lengths and time scales. However, before addressing such a level of complexity, to date, no univocal model describes the dynamics of the interaction between a single vortical structure and an inertial particle. In particular, evaluating the relative contribution of the different hydrodynamic forces acting on the particle is not straightforward (Calzavarini *et al.* 2009; Homann & Bec 2010). Consequently, the study of interactions between a single particle and a canonical vortical flow is a first step to address the fundamental physical mechanisms.

One of the most common coherent vortical structures is the vortex ring, which can be generated when an impulsive fluid motion occurs. For instance, these structures can be observed at the geophysical scale as smoke rings during volcanic eruptions (Pulvirenti *et al.* 2023), or in the internal convective movements of solar-type stars in the form of plumes (Dintrans *et al.* 2005). In terms of biological systems, vortex rings can be seen in numerous propulsion mechanisms, including the wakes of fish and jellyfish (Linden & Turner 2004; Dabiri 2009), as well as in pulsed systems such as the heart (Arvidsson *et al.* 2016). Regarding industrial applications, vortex rings are generated by rotating mechanical agitators or injection systems (Bouremel & Ducci 2017). Regardless of how they are generated, these coherent vortical structures are self-propagating, and transport mass and momentum along their trajectory, making them good candidates for agitation and dispersion (see Olsthoorn & Dalziel 2018). Moreover, vortex rings are often used as basic elements to generate a state of turbulence (Matsuzawa *et al.* 2023) and to study the interaction between turbulent vortices (McKeown *et al.* 2020). Consequently, these vortical structures, generic and universal, are often naturally chosen as a canonical flow to understand turbulence or more complex flows.

In addition, investigating interactions between vortex rings and particles in a controlled fashion may also be an opportunity to explore engineering applications. In this way, the work of An *et al.* (2016) presents a solution to bio-encapsulation of cells by freezing them into a vortex ring. Similarly, the vortex ring's ability to deliver inertial particles to targeted regions has been explored through vortex reconnection strategies using a point-like direct numerical simulation (Mouallem *et al.* 2021). Furthermore, the interaction between a vortex ring and bubbles was extensively studied, aiming to understand the interaction between turbulent eddies and bubbles in turbulent flows (Martínez-Bazán 2015). The interaction between bubbles and a vortex ring has been studied experimentally (Jha & Govardhan 2015), revealing modifications in both bubble and vortex ring dynamics. The role played by the deformability in that interaction is also investigated by comparing the bubble dynamics with a non-deformable element, a very low-density buoyant sphere (Biswas & Govardhan 2022). Building on this, recent experiments by Biswas & Govardhan

(2025) examined the interaction of low-density spherical particles with a vortex ring, demonstrating that the particle-to-ring-core size ratio plays a role in the interaction. Nevertheless, extending such investigations to other dynamical configurations is essential, as it allows for a systematic reduction of complexity, and provides new insights into vortex ring–particle interactions.

The present study aims to investigate the interaction between laminar vortex rings and a slightly buoyant (inertial) particle rising vertically, focusing on the effects of the particle's relative radial position with respect to the vortex axis of symmetry and the strength of the vortex ring. An experimental investigation enables us to (i) identify several interaction regimes and (ii) map those regimes as a function of the relevant parameters of the study. Then numerical simulations were performed on the basis of the experiments. This allows the identification of the hydrodynamic forces responsible for the particle dynamics in the interaction regime. The paper is organised as follows. The dynamical system and the experimental set-up are detailed in § 2. The vortex ring's experimental characterisation, with and without the presence of a particle, is detailed in § 3. The identification, description and mapping of the several interaction regimes are highlighted in § 4. The numerical simulations reproducing the experiments and allowing access to the dynamics are detailed in § 5. Finally, § 6 gives concluding remarks and perspectives on this work.

## 2. Tracking the interaction between a vortex ring and a particle

### 2.1. Description of the problem

A single spherical inertial particle (hereafter, particle refers to a finite spherical element of well-defined properties) evolving in the vicinity of a vortex ring is considered. The surrounding Newtonian fluid has constant density  $\rho_f$  and dynamic viscosity  $\mu_f$ . An overview of the dynamical system is presented in figure 1.

Vortex rings exhibit rotational symmetry and can therefore be modelled by tori (Tinaikar, Advait & Basu 2018) propagating by self-induced effect along their axis of symmetry. Here, the vortex ring propagates downwards along the vertical  $y$ -axis. The  $x$ - and  $z$ -axes belong to any horizontal plane and follow right-handed coordinates. The vortical structure is located at  $(x_{VR}, y_{VR}, z_{VR})$  and is characterised by three parameters: circulation  $\Gamma$ , diameter  $D_{VR}$ , and core radius  $a$  (Didden 1979; Gharib, Rambod & Shariff 1998). The vorticity distribution in the core is assumed to be Gaussian-like (Saffman 1970), and the streamwise vortex propagation velocity  $U_{VR}$  is deduced from the above-mentioned parameters. Those few features make the vortex ring a simple and controllable coherent structure (Jha & Govardhan 2015; Qi *et al.* 2022).

The particle is a sphere with diameter  $d_p$  and density  $\rho_p < \rho_f$  moving at velocity  $U_p$ . While evolving freely, it follows a rectilinear motion resulting from the balance between buoyancy and drag forces, leading to a terminal rising velocity. The particle vertical position is denoted  $y_p$ , and its localisation in the horizontal plane  $(x_p, z_p)$  can be reduced to its radial position relative to the vortex ring propagation axis,  $r_p$ . The particle is initially released at a given radial position  $r_{rel} = ((x_p - x_{VR})^2 + (z_p - z_{VR})^2)^{1/2}$ .

### 2.2. Experimental set-up

A sketch of the experimental set-up is shown in figure 2. During the experiment, the room temperature is controlled at 20 °C, and the fluid properties are assumed to be constant,  $\rho_f = 998 \text{ kg m}^{-3}$  and  $\mu_f = 0.001 \text{ Pa s}$ . At the top of a water-filled tank with dimensions

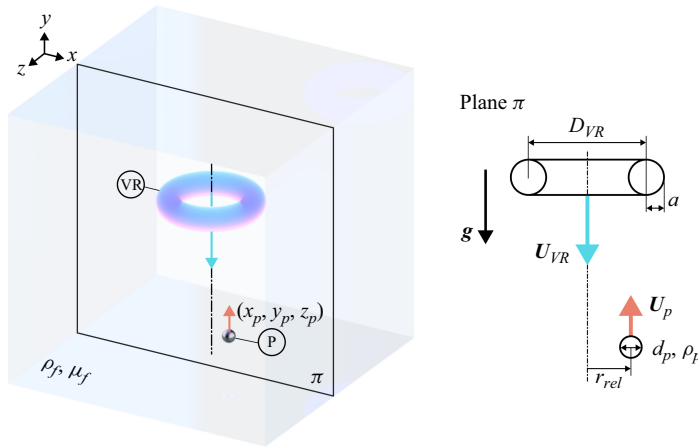


Figure 1. Schematic of the dynamical system where both the vortex ring  $\textcircled{\text{VR}}$  and the particle  $\textcircled{\text{P}}$  are represented. The surrounding Newtonian fluid has constant density  $\rho_f$  and viscosity  $\mu_f$ . The system's main parameters are present in the vertical symmetry plane  $\pi$ . The particle  $\textcircled{\text{P}}$  (diameter  $d_p$ , density  $\rho_p$ ) is released at a given distance from the  $\textcircled{\text{VR}}$  propagation axis  $r_{\text{rel}}$ , and evolves along the gravity axis at velocity  $U_p$ . The vortex ring  $\textcircled{\text{VR}}$  (diameter  $D_{VR}$ , core size  $a$ ) propagates along the  $y$ -axis at velocity  $U_{VR}$ .

$W \times L \times H = 50 \times 50 \times 90 \text{ cm}^3$ , a vortex ring is generated using a piston–cylinder apparatus (shown in figure 2a). The same generation strategy has been used in various studies (e.g. Maxworthy 1977; Didden 1979; Sullivan *et al.* 2008; Pinaud *et al.* 2021). A piston is translated by a linear actuator in a cylinder of diameter  $D_g = 2 \text{ cm}$  (hereafter, the subscript  $g$  stands for ‘generator’ of the vortex ring), resulting in a starting jet at the exit that rolls up to generate the vortex ring. The piston velocity  $U_g$  is set to be a top-hat function. It accelerates to the target velocity  $\overline{U}_g$  within a few milliseconds, sustains this constant velocity over the stroke duration  $t_g$ , and subsequently decelerates to rest within a comparable time scale. The piston position is measured by a magnetic ruler, sampled at frequency 1000 Hz. The piston stroke time is related to the piston velocity so that  $t_g = 3D_g/U_g$  in order to avoid the formation of a secondary vortex ring (Gharib *et al.* 1998). An example of the measured piston displacement and the velocity derived from it is shown in figure 2(b). The cylinder is a perspex tube whose end has been chamfered to facilitate the winding of the vorticity sheet at the tube outlet to create the vortex ring (bevel angle approximately  $75^\circ$ ). In addition, the cylinder is immersed  $5D_g$  below the free surface to avoid any interaction between the free surface and the vortical structure (Bentata, Anne-Archard & Brancher 2018; Pinaud *et al.* 2021; Albagnac & Anne-Archard 2024). The cylinder symmetry axis is the vertical  $y$ -axis, and the spatial origin of the system  $O$  is located on this axis at the cylinder exit. The time initialisation,  $t = 0$ , is set at the end of the piston motion. The characteristics of the vortex ring resulting from this configuration, as detailed later in figure 4, corroborate previous results (Didden 1979; Gharib *et al.* 1998; Pinaud *et al.* 2021), namely a propagation velocity and a diameter both proportional to the piston–cylinder apparatus characteristics.

A dedicated device was built to release the particle from the bottom of the tank. This device is composed of a rigid structure supporting a perspex cone whose apex, pointing upwards, is truncated (dark grey particle releaser in figure 2c). A pneumatic stick at the top of the cone maintains the buoyant particle under it. Then, when the stick is activated, it releases the particle, which rises in the tank under buoyant effect. The particle, manufactured by a three-dimensional printer, is a hollow sphere with external



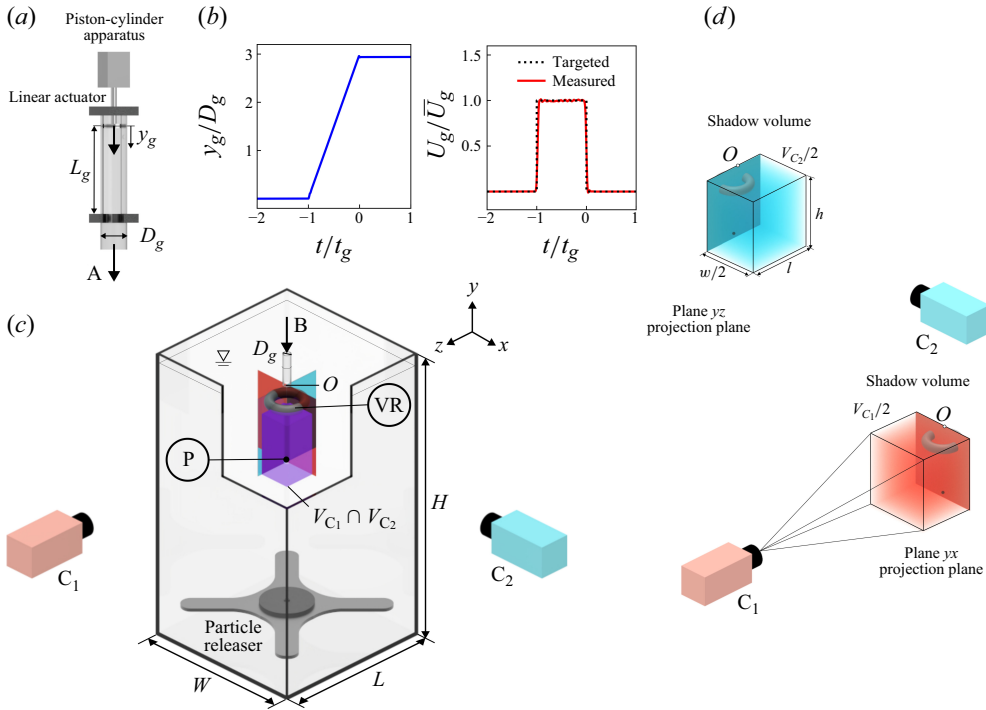


Figure 2. Schematic of the experimental set-up for analysing the interactions between a vortex ring  $\textcircled{v}$  and a particle  $\textcircled{p}$ . (a) Overview of the piston–cylinder apparatus, used to generate the vortex ring, with  $D_g$  representing the piston diameter,  $L_g$  the stroke length, and  $U_g$  the piston velocity. A linear actuator drives the piston, while a magnetic ruler measures its displacement, shown in (b). The piston velocity is set to be a top-hat function, where the piston reaches a plateau velocity  $\bar{U}_g$  for a stroke time  $t_g$ . The initialisation time ( $t = 0$ ) is established at the end of the piston stroke. The exit of the piston–cylinder apparatus is linked via a flexible tube to a rigid tube submerged in the tank (A to B). (c) The vortex ring is generated in a tank with dimensions  $W \times L \times H = 50 \text{ cm} \times 50 \text{ cm} \times 90 \text{ cm}$ . A pneumatic particle releaser enables the controlled release of the particle from the bottom of the tank. The  $\textcircled{v}$  and  $\textcircled{p}$  trajectories are monitored via shadowgraphy using two cameras that are orthogonal to each other,  $C_1$  and  $C_2$ . (d) A detailed representation of the volumetric field of view: the cameras capture a volumetric region of dimensions  $25 \text{ cm} \times 23 \text{ cm} \times 25 \text{ cm}$ , projected in the  $yx$  and  $yz$  planes, intersecting along the axis of the immersed cylinder. The representation of the volumetric intercepted region is  $V_{C_1} \cap V_{C_2}$  (purple area in (c)).

diameter  $d_p = 5 \text{ mm}$  and inner diameter  $2.9 \text{ mm}$ . The relative density of the particle is  $\rho_p/\rho_f = 0.989$ . The vertical position of the release system is sufficiently far from the vortex ring generator for the particle to reach its terminal rising velocity before interacting with the vortex ring. The same particle is used for all the experimental runs. Finally, the relative initial radial position of the particle,  $r_{rel}$ , is varied by displacing the vortex ring cylinder along the horizontal  $x$ -direction while the particle release system remains at the same place.

The three-dimensional trajectory of the particle is obtained by shadow monitoring (Fernandes *et al.* 2007). Two synchronised sCMOS cameras equipped with a 105 mm F11 lens, orthogonal to each other and with depth of field  $w = 25 \text{ cm}$ , image the volume of interest. The acquisition frequency is set to 50 frames per second. The vertical projection of the imaged volume is  $l \times h = 23 \times 25 \text{ cm}^2$  along the horizontal and vertical directions, respectively, and the spatial resolution is approximately  $100 \text{ px cm}^{-1}$ . The central vertical line of the images obtained by the two cameras coincides with the axis of the particle releaser cone. The imaged area includes the exit of the cylinder

(see schematic diagram in [figure 2d](#)). The visualisation apparatus enables tracking of both the vortex ring centre, visualised with fluorescein (dye Schmidt number  $Sc_{dye} \approx 2000$ ), and the particle trajectory. The vortex centre is determined by detecting the vortex ring contour from the grey intensity gradient and computing the iso-barycentre of the enclosed region. This procedure follows the approach described in Fernandes *et al.* (2007). Camera C<sub>1</sub> (plane  $yx$ ) gives the coordinates  $y$  and  $x$ . Complementarily, camera C<sub>2</sub> tracks the projection in the plane  $yz$ , giving the coordinates  $y$  and  $z$ . Then, combining those projections at a given time  $t_i$  by matching the particle's vertical position  $y_p$ , the complete three-dimensional position  $(x_p(t_i), y_p(t_i), z_p(t_i))$  is obtained. Finally, particle velocity and acceleration are computed from convolution with Gaussian kernels, as suggested by Zimmermann *et al.* (2011) and Mathai *et al.* (2016).

The visualisation campaign was complemented by two-dimensional two-component time-resolved particle image velocimetry (TR-PIV) realised in a vertical symmetry plane of the vortex ring. The complete characterisation of the vortical structure, with or without interaction with the particle, is thus assessed, namely the time evolution of its diameter  $D_{VR}(t)$ , its propagating velocity  $U_{VR}(t)$ , the size of its core  $a(t)$ , and its circulation  $\Gamma_{exp}(t)$ . The camera used for the TR-PIV is a Dimax equipped with a 105 mm F11 lens, with maximum acquisition frequency 1000 Hz. The size of the field is  $l \times h = 20 \times 20 \text{ cm}^2$ , and the spatial resolution is approximately  $100 \text{ px cm}^{-1}$ . Hollow glass spheres of diameter  $10 \text{ }\mu\text{m}$  and density  $1.1 \text{ g cm}^{-3}$  are used to seed the flow, and are illuminated by a 1 mm thick laser sheet (Nd:YLF laser, wavelength 527 nm). The TR-PIV was also performed for a vortex ring interacting with a particle. For this configuration, fluorescent Rhodamine-B particles of diameter  $21.4 \text{ }\mu\text{m}$  and density  $1.03 \text{ g cm}^{-3}$  were used, and a high-pass filter (540 nm cut-off wavelength and optical density OD 4) was applied to the camera lens. This approach was necessary due to the high reflection of the laser beam when the particle crosses the laser sheet. The velocity vectors were computed using Davis PIV software with a multi-pass cross-correlation algorithm in a total of four passes starting in an interrogation box window of  $64 \times 64 \text{ px}^2$  (50 % overlap) with a final interrogation window of  $16 \times 16 \text{ px}^2$  (75 % overlap), resulting in PIV grid spacing approximately 0.4 mm.

### 2.3. Parameters governing the vortex ring and particle interaction

From the different parameters defined in § 2.1, six dimensionless numbers are necessary to describe the configuration illustrated in [figure 1](#):

$$Ga \equiv \frac{v_g}{v_v} = \frac{\left[ |(\rho_p/\rho_f) - 1| g d_p^3 \right]^{1/2}}{v_f}, \quad (2.1)$$

$$Re_{VR} \equiv \frac{\tau_v}{\tau_i} = \frac{\rho_f U_{VR} D_{VR}}{\mu_f}, \quad (2.2)$$

$$St_p \equiv \frac{\tau_p}{\tau_f} = \frac{\rho_p d_p^2 / 18 \mu_f}{D_{VR} / U_{VR}}, \quad (2.3)$$

$$R_r \equiv r_{rel} / D_{VR}, \quad (2.4)$$

$$\rho_p / \rho_f, \quad (2.5)$$

$$2a / D_{VR}, \quad (2.6)$$

where  $Ga$  is the Galileo number (also referred to as the Archimedes number, for instance, in Ern *et al.* 2012) associated with the particle, which compares the buoyancy-driven velocity scale  $v_g \equiv [|\rho_p/\rho_f - 1| d_p g]^{1/2}$  with the viscous velocity scale  $v_v \equiv \nu_f/d_p$  (Brandt & Coletti 2022). The vortex ring Reynolds number  $Re_{VR}$  is defined as the ratio of an inertial time scale  $\tau_i \equiv D_{VR}/U_{VR}$  to a viscous time scale  $\tau_v \equiv \rho_f D_{VR}^2/\mu_f$ . For simplicity, the vortex ring velocity  $U_{VR}$  is used here to define the Reynolds number instead of the circulation  $\Gamma$  (as in Maxworthy (1972) and Olsthoorn & Dalziel (2018)). The Stokes number  $St_p$  is defined as the ratio of the particle response time to a change in the surrounding fluid and the characteristic flow field time scale. Assuming a Stokes drag, the particle response time can be expressed as  $\tau_p \equiv \rho_p d_p^2/(18\mu_f)$  (Brandt & Coletti 2022), while the flow time scale is simply  $\tau_f \equiv \tau_i$ . The non-dimensional released position of the particle,  $R_r$ , is the distance from the vortex ring symmetry axis  $r_{rel}$  relative to the vortex ring length scale  $D_{VR}$ . The relative density is  $\rho_p/\rho_f$ , and  $2a/D_{VR}$  is the vortex ring compactness.

In this study, since the particle used is always the same,  $d_p$  and  $\rho_p$  are constant, which fixes the Galileo number  $Ga = 110$  and  $\rho_p/\rho_f$ . The particle characteristics are selected so that its rising motion is as vertical and steady as possible before entering the experimental field of view (Zhou & Dušek 2015). Here, three Reynolds numbers  $Re_{VR}$  have been explored, and consequently three Stokes numbers  $St_p$ . The range of Reynolds explored is high enough for the vortex ring to be inertial, and low enough to ensure the morphological stability of the coherent structure (Widnall & Sullivan 1973). In addition, the particle trajectory was initiated at four different positions relative to the propagation axis of the vortex ring  $r_{rel}$ . It is important to note that while the particle's release position relative to the cylinder axis is fixed for a specific configuration, the particle's radial position upon first encountering the vortex ring can differ even within the same configuration. When the pneumatic stick releases the particle, it may introduce minor perturbations, such as translation or rotation, which can cause the particle's initial trajectory to deviate from a perfectly vertical path. Consequently, the particle's relative radial position considered is the actual position measured experimentally when the particle is  $1.5D_{VR}$  below the vortex ring centre.

The values of the dimensionless parameters covered by the study are given in table 1. As mentioned earlier, the vortex ring is generated using a piston–cylinder apparatus, and its characteristics are directly linked to this apparatus (explained further in § 3). The controlled parameters correspond to those of the piston–cylinder system. Consequently, the Reynolds number is defined based on these controllable parameters as  $Re_g \equiv \bar{U}_g D_g \rho_f / \mu_f$ . Additionally, the radial position of the particles relative to the vortex ring axis is normalised by the cylinder diameter  $D_g$ . In addition to those parameters, the vortex ring characterisation was extended for two other generator Reynolds numbers, 1200 and 3000 (see § 3). The vortex ring properties derived from this analysis enable extending further the analysis in the numerical simulation presented in § 5 for another two Stokes numbers, 1.6 and 3.9. The numerical results are also extended to several values of  $R_r$  in a similar range.

### 3. Vortex ring dynamics

The TR-PIV was performed in the vertical symmetry plane of the vortex ring for three different piston velocities  $\bar{U}_g = 9, 12, 18 \text{ cm s}^{-1}$  corresponding to  $Re_g = 1800, 2400, 3600$ . Each configuration was reproduced three times with and without particle interaction in order to check the repeatability of the experiments and evaluate the possible

| Cases | $Re_g$ | $r_{rel}/D_g$    | $St_p$ | $\rho_p/\rho_f$ | $Ga$ |
|-------|--------|------------------|--------|-----------------|------|
| A     | 1800   |                  | 2.4    |                 |      |
| B     | 2400   | 0, 0.5, 1.0, 1.5 | 3.2    | 0.989           | 110  |
| C     | 3600   |                  | 4.7    |                 |      |

Table 1. Dimensionless parameters covered by the study. The Reynolds number  $Re_g \equiv \overline{U}_g D_g \rho_f / \mu_f$  is based on the piston–cylinder apparatus used to generate the vortex ring. The Stokes number  $St_p \equiv \tau_p / \tau_f$  is a ratio between the particle response time and the vortex ring time scale. Here,  $r_{rel}/D_g$  is the radial distance between the particle and the vortex ring axis normalised by the cylinder diameter ( $D_g = 20$  mm),  $\rho_p/\rho_f$  is the density ratio between the particle and the fluid, and  $Ga$  is the Gallileo number.

effect of the particle on vortex ring dynamics. Note that two additional piston velocities were tested to further characterise the vortex ring without particle interaction,  $\overline{U}_g = 6, 15$ , leading to  $Re_g = 1200, 3000$ .

### 3.1. Properties of a vortex ring propagating without particle interaction

Typical information extracted from the TR-PIV measurements is shown in figure 3, where all the quantities are non-dimensionalised by the vortex ring generation parameters, namely,  $D_g$  and  $\overline{U}_g$ . Figure 3(a) shows the in-plane components of the velocity (black arrows) on top of the streamwise velocity magnitude (colour). The streamwise velocity profile on the left of figure 3(a) (solid black line) is obtained by averaging the profiles along different PIV grid nodes in the spanwise direction over  $x/D_g \in [-0.5, 0.5]$ , and the standard deviation is shown in red. This averaging smooths small deviations or experimental noise, as the vortex ring axis is not necessarily aligned with a vertical PIV grid line. The standard deviation indicates only small differences between the profiles. The vertical position of the vortex ring core,  $y_{VR}(t)$ , is located at the maximum of the averaged streamwise velocity (Pinaud *et al.* 2021).

The vertical velocity along the spanwise direction at the vertical position is then calculated (bottom of figure 3a). The propagation velocity of the coherent structure,  $\overline{U}_{VR}$ , is obtained by computing the time derivative of  $y_{VR}(t)$  after applying a least squares fit for  $t \in [1, 4] t_g$  ( $R^2 > 0.99$ ). The vortex ring diameter  $D_{VR}(t)$  is defined as the distance separating the two zero-crossing points of this velocity profile (blue dots) in the vortex ring reference frame ( $u_y - \overline{U}_{VR}$ ). The vortex ring propagation velocity is approximately  $0.6 \overline{U}_g$ , as also reported by other studies that used the same apparatus (Pinaud *et al.* 2021) and a similar vortex ring piston–cylinder generation technique (Didden 1979), which supports the method to measure  $D_{VR}$  shown in figure 3.

The computation of the vorticity  $\omega_z(x, y)$  (see figure 3b) requires evaluation of the velocity gradient. For this purpose, the velocity components, obtained directly by PIV, are fitted on a five-five stencil with a second-order polynomial function and then spatially differentiated (Fouras & Soria 1998). This approach reduces the experimental error and is more robust than a simple central finite differentiation. Figure 3(c) shows iso-contours of vorticity in the vicinity of the vortex ring core. The vortex ring core radius  $a$  and circulation  $\Gamma_{exp}(t)$  are calculated from regions bounded by iso-contours  $C_n$  ( $\omega_z = 0.1\omega_{z,min}$ ) and  $C_p$  ( $\omega_z = 0.1\omega_{z,max}$ ) for the negative and positive vorticity, respectively. The circulation results from the vorticity integration within the contour using the central finite-difference method. The vortex ring core is estimated with the second moment method calculated in the zone delimited by this same iso-contour

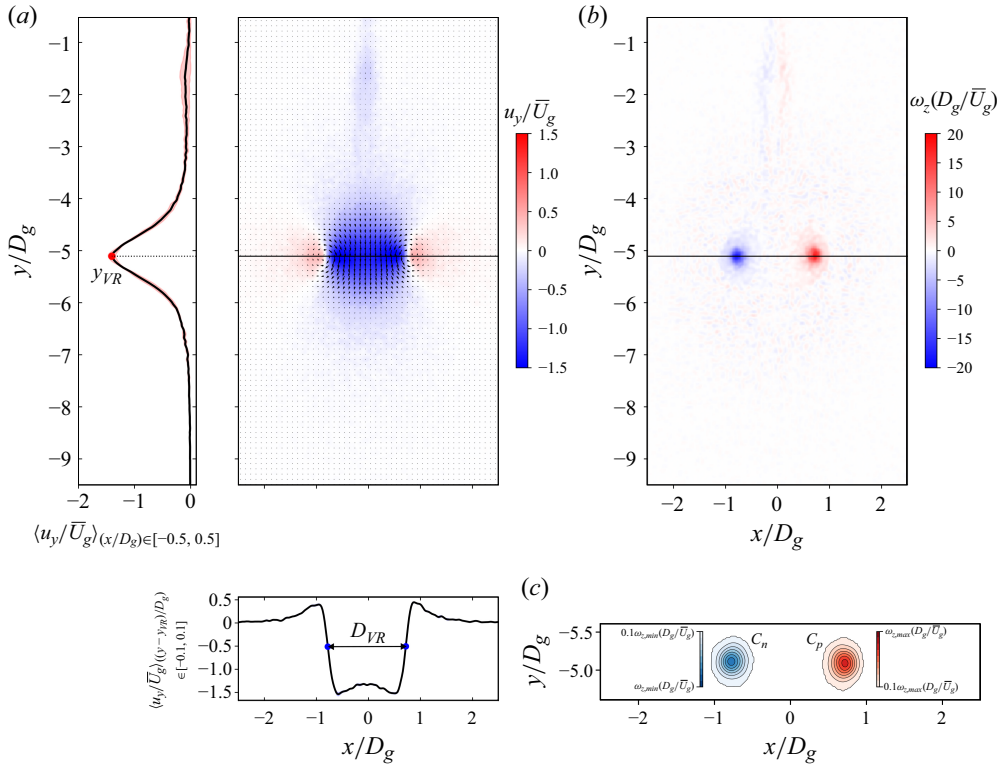


Figure 3. Results extracted from TR-PIV measurements at a specific time  $t/t_g = 2.00$ . (a) Colour map of the streamwise velocity magnitude  $u_y/\bar{U}_g$  along with the in-plane velocity field (black vectors). On the left-hand side of (a), the streamwise velocity averaged over  $x/D_g \in [-0.5, 0.5]$  is shown as a black line, with its standard deviation indicated in red. The vertical position of the vortex ring centre  $y_{VR}$  is marked with a red dot. At the bottom, the streamwise velocity averaged over  $(y - y_{VR})/D_g \in [-0.1, 0.1]$  is shown as a black line, with the corresponding standard deviation in blue. The vortex ring diameter  $D_{VR}$  is indicated by an arrow. (b) The vorticity field, while iso-contours of negative and positive vorticity ( $C_n$  and  $C_p$ ) are detailed in (c), which are used to determine the vortex core size and circulation.

(Le Dizès & Verga 2002):

$$a^2 = \frac{1}{\Gamma_{exp}} \iint_S [(x - x_c)^2 + (y - y_c)^2] \omega_z(x, y) dx dy, \quad (3.1)$$

where  $x_c$  and  $y_c$  are the coordinates of the iso-contour barycentre given by  $x_c = 1/\Gamma_{exp} \iint_S x \omega_z(x, y) dx dy$  and  $y_c = 1/\Gamma_{exp} \iint_S y \omega_z(x, y) dx dy$ , respectively, and  $S$  is the surface of the region delimited by  $C_n$  (or  $C_p$ ). The core radius is estimated at a given time in both positive and negative regions, and the mean value is retained.

An overview of the previously mentioned parameters extracted from the measurements on a vortex ring propagating without particle interaction is presented in figure 4. Note that the vortex ring properties are calculated once the vortex is fully developed, which is assumed to occur for  $y/D_g \leq -3$  (i.e. the vortex ring has travelled over a typical piston stroke length). Over the field of view (approximately nine cylinder diameters), the vortex ring dynamics is expected to be controlled by inertia, and time is therefore normalised by the generator time scale  $t_g = 3D_g/U_g$ .

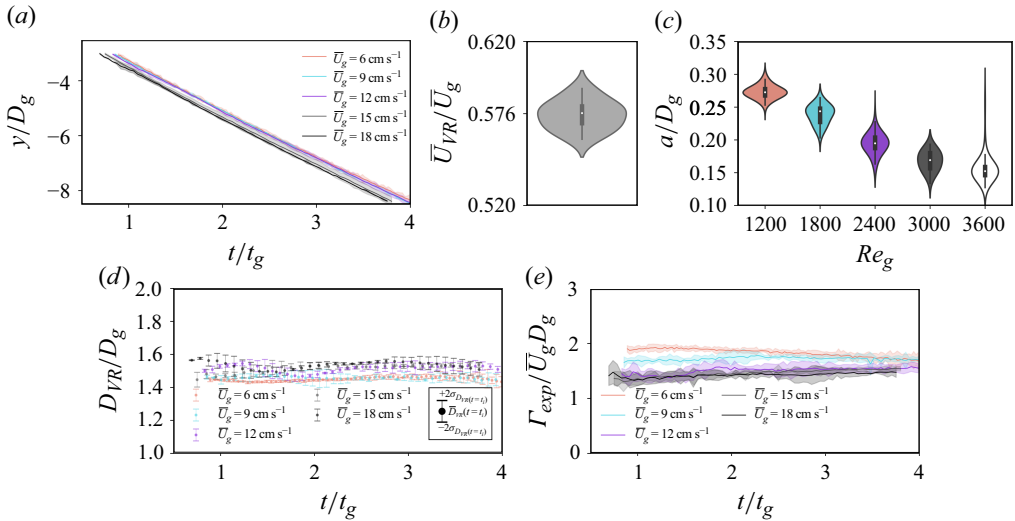


Figure 4. Statistical characterisation of vortex rings properties for different piston velocities  $\bar{U}_g$ . (a) Time evolution of vortex ring streamwise position. (b) Violin plot of the distribution of vortex ring propagation velocity in all experiments. (c) Violin plots of vortex ring core size distribution at all times as a function of the Reynolds number  $Re_g$ . (d) Time evolution of the vortex ring diameter. (e) Time evolution of the vortex ring circulation. Shadow regions and error bars represent twice the standard deviation. The violin plot combines a box plot with a probability density estimate, showing summary statistics (median, interquartile range) and the shape of the data distribution (Hintze & Nelson 1998).

The time evolution of the vortex ring streamwise position for several piston velocities is presented in figure 4(a). Solid lines are obtained by averaging three independent runs realised with the same generating parameters and previously synchronised, while shadow regions show twice the standard deviation. The streamwise position  $y/D_g = -3$  is reached after one generator time  $t_g$  for the higher Reynolds numbers, but it could take more time for the lowest ones. Then whatever the Reynolds number, the streamwise evolution of the vortex ring is linear with a constant slope corresponding to the propagating velocity. Therefore, once generated and fully developed (i.e. for  $y/D_g \leq -3$ ), the vortex ring dynamics is inertial. The low dispersion of the probability distribution of the vortex propagation velocity (see figure 4b) reveals the strong repeatability of the experiments. In agreement with previous experimental studies (Didden 1979; Sullivan *et al.* 2008), the vortex ring propagation velocity is directly linked to the piston velocity  $U_g$  by  $\bar{U}_{VR}/\bar{U}_g = 0.576 \pm 0.009$ .

The core size distribution and the time evolution of the diameter of the vortex ring are shown in figures 4(c) and 4(d), respectively. The diameter of the vortex ring is independent of piston velocity, and exhibits a slight increase over time. This expansion is related to viscous diffusion and entrainment of the ambient fluid, which is present, albeit at a low level, during the propagation (Maxworthy 1972; Sullivan *et al.* 2008; Tinaikar *et al.* 2018). Nevertheless, this variation is marginal over the field of view, and the vortex ring diameter will be assumed constant in the following,  $D_{VR}/D_g \approx 1.5$ . As shown in figure 4(c), the Gaussian-like probability distribution, along with the small dispersion, indicates that the vortex ring core size barely changes during the propagation. However, the core size decreases with the Reynolds number. Finally, the time evolution of the vortex ring circulation is presented in figure 4(e) and shows that the circulation is globally constant over the recording.



### 3.2. Properties of vortex rings interacting with a particle

In order to evaluate the potential influence of the particle on the parameters that characterise the vortex ring, a comparison of the velocity field and the vortex ring properties with and without interaction with the particle is presented in [figure 5](#). Several regimes may occur, depending on the vortex properties and the initial release condition of the particle, resulting in short-lived interactions or sustained ones over time, as discussed later, in § 4. To assess whether the particle can affect the vortex ring dynamics, the interaction regime is considered in which the particle remains entrained within the vortex for an extended duration (hereafter referred to as the capture regime), i.e. until it exits the field of view.

[Figure 5\(a–c\)](#) show a direct comparison of the velocity field associated with the vortex ring with and without particle interaction for the same vortex generation parameters at three different times:  $t/t_g = 1.47$  (I),  $t/t_g = 2.40$  (II), and  $t/t_g = 4.00$  (III). Except in the immediate vicinity of the particle, the velocity field does not appear to be qualitatively affected by the particle, its magnitude being the same. For a more precise quantification, [figure 5\(g\)](#) displays the averaged velocity profile (solid line) along the spanwise direction at the vortex core's streamwise position. This profile is averaged over time for  $t/t_g \in [1.47, 4.00]$ . The shadowed region indicates the standard deviations for these configurations, both with and without interaction. The influence of the interaction over time is evaluated in [figure 5\(d–f\)](#), which show the temporal evolutions of the ring's vertical position, diameter and circulation with and without the presence of the particle. The influence of the particle is not noticeable on the vortex properties. As a result, while the particle is influenced by its interaction with the vortex ring, the coherent structure is only slightly affected by the particle. In a similar configuration, experiments conducted by Biswas & Govardhan (2025) investigated the effect of the particle-to-ring-core diameter ratio ( $d_p/2a$ ) on the interaction between a vortex ring and a very light particle with density ratio  $\rho_p/\rho_f = 0.008$ . It was observed that when the particle-to-ring-core diameter ratio exceeds unity, the influence of the particle on vortex dynamics becomes more pronounced. Despite key differences between the studies – including variations in experimental set-up, density ratios, particle rising regimes and vortex ring strengths – the findings presented here are somewhat corroborated. The particle-to-ring-core diameter ratio in this present study lies in the range  $d_p/2a \in [0.45, 0.80]$ . However, the impact of the density ratio and particle rising regimes on this interaction remains an open question. Further, three-dimensional measurements or fully coupled numerical simulations would be of high interest.

## 4. Kinematics of the particle in the vicinity of the vortex ring

As previously mentioned, several interaction regimes are observed, depending on the properties of the vortex ring and the initial position of the particle relative to the vortex axis of propagation. For the range of parameters explored in the present study, three distinct regimes were observed: simple deviation, strong deviation and capture. A description of these regimes is given hereafter.

### 4.1. Simple deviation

[Figure 6](#) gives an overview of the kinematics of a particle in a simple deviation regime. This regime is characterised by a weak radial deviation in the particle's upward trajectory. The particle trajectory is presented at three different times in [figure 6\(a\)](#). In the following, the time is systematically non-dimensionalised by  $\tau_i = D_{VR}/U_{VR}$  in order to have a

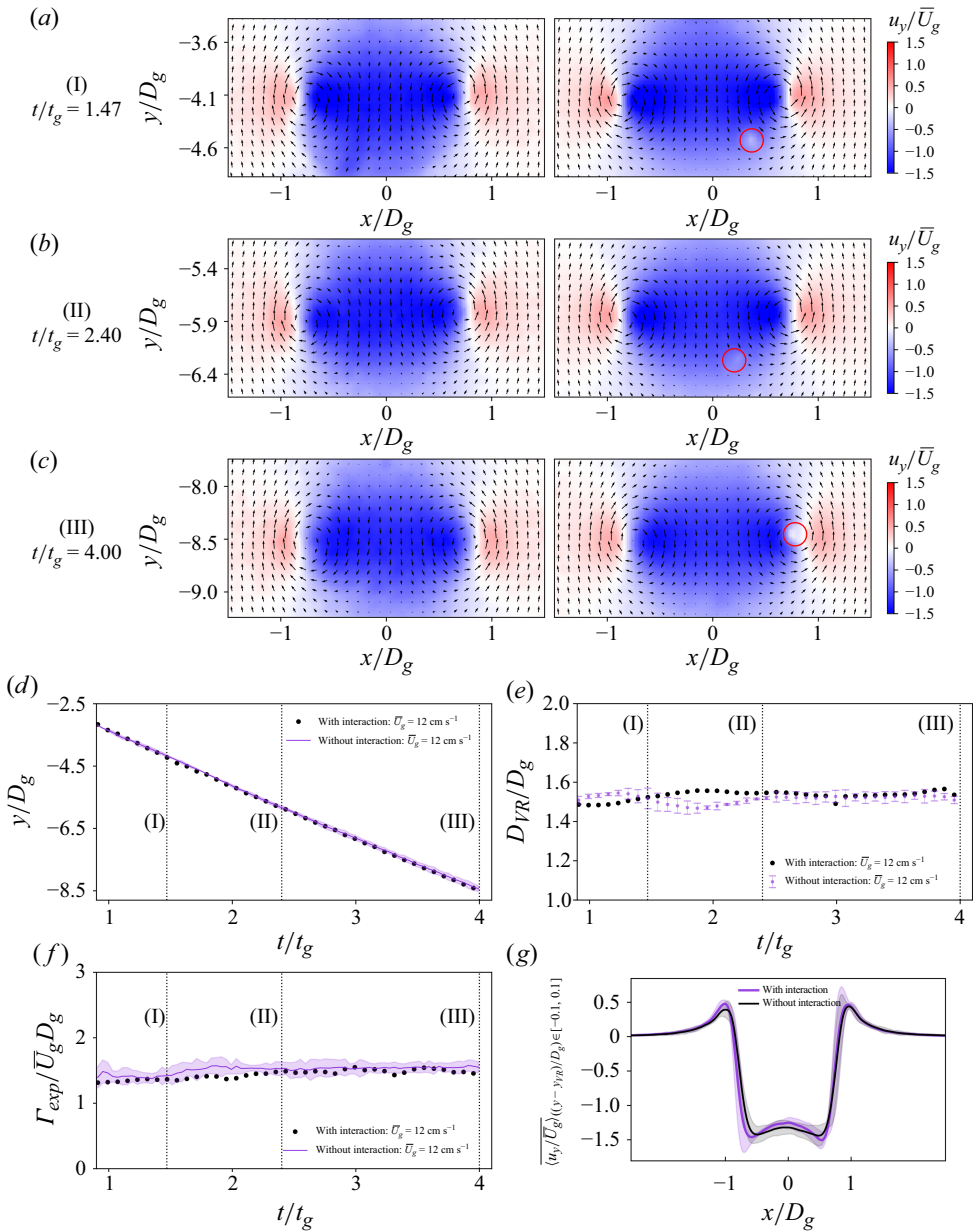


Figure 5. Comparison of the vortex ring characteristics with and without particle interaction under the capture regime for  $\bar{U}_g = 12 \text{ cm s}^{-1}$ . (a–c) The in-plane velocity field centred on the vortex ring position (black arrows, with one arrow shown for every five experimental points in both directions), along with the streamwise velocity magnitude (colour) without (left) and with (right) particle interaction for three times:  $t/t_g = 1.47$  (I) in (a),  $t/t_g = 2.40$  (II) in (b), and  $t/t_g = 1.47$  (III) in (c). Time evolutions of (d) the vertical position of the vortex ring, (e) the vortex ring diameter, and (f) the circulation. (g) The velocity profile averaged in time ( $t/t_g \in [1.47, 4.00]$ ) for both cases.

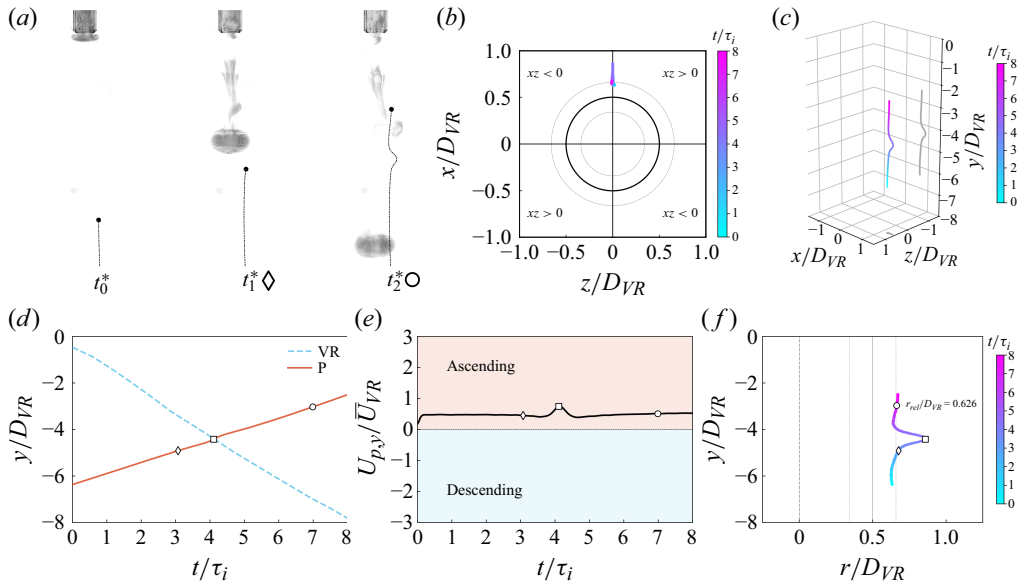


Figure 6. Particle kinematics under simple deviation regime  $R_r = 0.626$ ,  $St_p = 2.2$ . (a) Snapshots from experiments corresponding to three different time instances:  $t_0^*$ ,  $t_1^*$  and  $t_2^*$ . (b) Time evolution of the particle position projected in the  $xz$  plane. (c) Three-dimensional spatial reconstruction of the particle's trajectory based on shadowgraphy measurements. (d) Time evolution of the vertical position  $y$  of both the particle (P) and the vortex ring (VR). (e) Time derivative of the particle trajectory. (f) The trajectory in terms of radial and vertical position of the particle. In (d–f),  $t_1^*$  and  $t_2^*$  are marked with diamond and circle symbols, respectively, while the square symbol indicates the moment when the particle and the vortex ring are at the same vertical position.

common definition of the characteristic time, as opposed to  $t_g$ , which referred to the experimental process of generating the vortex ring. The non-dimensional time is defined as  $t^* = t/\tau_i$ . Time  $t_0^*$  represents the initial state at which the particle rises at its terminal velocity, and is not affected by the vortex ring yet. At  $t_1^*$ , the particle is  $1.5D_{VR}$  below the vortex ring. This time is expected to correspond to the beginning of the interaction. At  $t_1^*$ , the particle deviates horizontally. The long-time interaction is defined as  $t_2^* = t_1^* + 3$ , where  $t/\tau_i = 3$  represents three times the characteristic advection time scale of the vortex. For the simple deviation regime, at  $t_2^*$ , the particle has recovered a vertical trajectory and travels at the terminal velocity.

The complete three-dimensional spatial reconstruction of the particle trajectory, derived from shadowgraphy measurements, is presented in figure 6(c). The time evolutions of the vertical position of both the vortex and the particle are represented in figure 6(d) where  $t_1^*$ ,  $t_2^*$  are indicated with diamond and circle symbols, respectively. A square symbol is added at the intersection of the particle and vortex ring trajectories. The corresponding time is referred to as  $t_{ce}^*$  (where *ce* stands for ‘complete encounter’). Additionally, the time evolutions of the particle positions projected in the  $xz$  plane are presented in figure 6(b), with auxiliary lines representing the vortex ring (the solid black circle represents the same radius as the vortex ring, and the dashed circles, separated by  $2a$ , illustrate its extension). The particle vertical velocity is shown in figure 6(e). The particle velocity, while influenced by the vortex ring when the particle is within its domain of influence, remains positive in time. This feature was observed for all the configurations ( $St_p$ ,  $R_r$ ), leading to simple deviations. The maximum velocity is reached when the particle is at the vertical level of the vortex ring core (square symbol). Finally, the particle radial displacement is shown in figure 6(f), where the vortex ring axis of symmetry

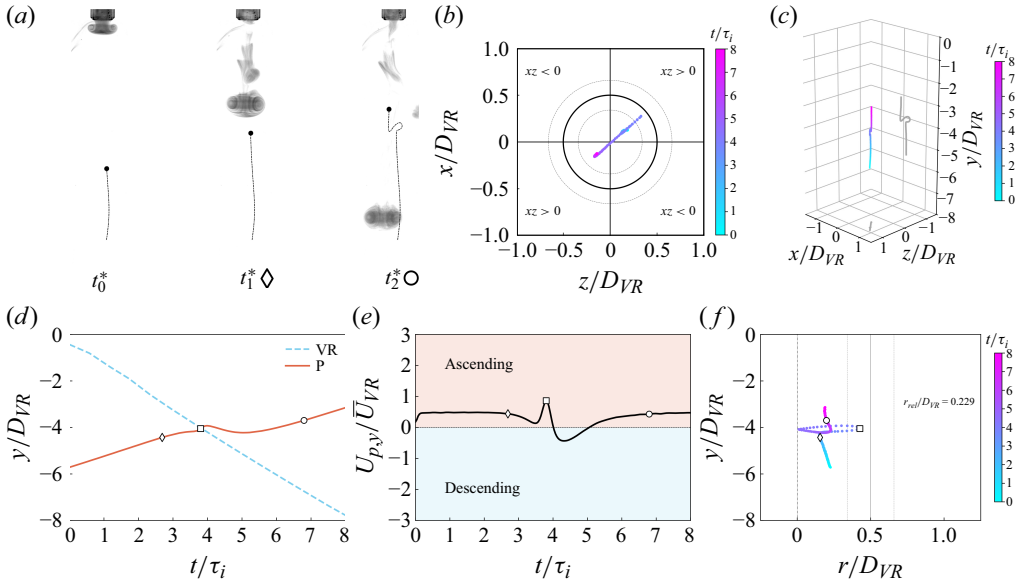


Figure 7. Particle kinematics under strong deviation regime  $R_r = 0.229$ ,  $St_p = 2.2$ . (a) Snapshots from experiments corresponding to three different time instances:  $t_0^*$ ,  $t_1^*$  and  $t_2^*$ . (b) Time evolution of the  $x$  and  $z$  particle positions. (c) Three-dimensional spatial reconstruction of the particle's trajectory based on shadowgraphy measurements. (d) Time evolution of the vertical position  $y$  of both the particle (P) and the vortex ring (VR). (e) Time derivative of the particle trajectory. (f) The trajectory in terms of radial and vertical position of the particle. In (d–f),  $t_1^*$  and  $t_2^*$  are marked with diamond and circle symbols, respectively, while the square symbol indicates the moment when the particle and the vortex ring are at the same vertical position.

is represented by the dash-dotted line  $r/D_{VR} = 0$ , and the solid black and dashed grey lines indicate the vortex core position  $r/D_{VR} = 0.5$  and its extension  $2a$ , respectively. The particle is radially deviated by the vortex when it passes near it, and then back near its initial radial position prior to the encounter. The condition for qualifying the regime as a simple deviation is defined as

$$U_{p,y}(t^*) > 0 \quad \forall t^* \in [0, t_2^*] \quad \wedge \quad \exists t^* \in [t_1^*, t_2^*] : \left| \frac{r_p(t^*) - r_p(t_1^*)}{D_{VR}} \right| > 0.075, \quad (4.1)$$

where the criterion  $|r_p(t^*) - r_p(t_1^*)/D_{VR}| > 0.075$  represents a non-negligible radial displacement (i.e. not vanishingly small). This threshold falls within the bounds of experimental uncertainty and is therefore used to classify the case as a simple deviation. While this condition is also important in other cases, it will not be restated with each criterion for the sake of simplicity.

#### 4.2. Strong deviation

An example of a strong deviation case is now presented in figure 7. For this configuration, the Stokes number is the same as for the simple deviation; only the initial radial position of the particle has changed. At  $t_1^*$ , the particle trajectory starts to be influenced by the vortex, and its rising velocity decreases (see figure 7d,e). As for the simple deviation regime, the particle experiences first a radial displacement away from the vortex ring centre between  $t_1^*$  and  $t_{ce}^*$  (represented by the diamond and square symbols, respectively). This radial displacement is also represented in figures 7(b) and 7(f). However, in this case, the trajectory of the particle is significantly influenced by the vortex ring as it moves towards

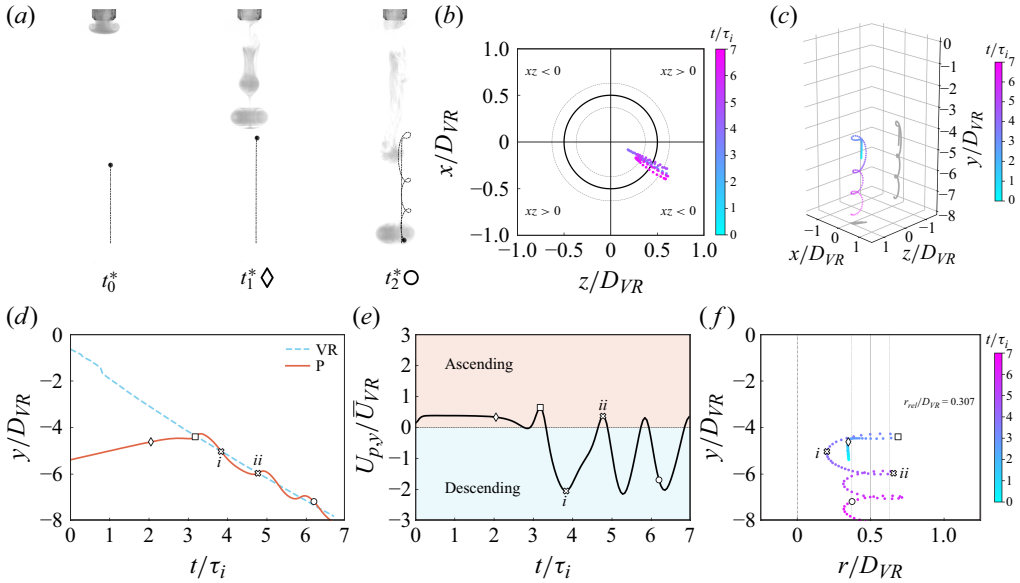


Figure 8. Particle kinematics under capture regime  $R_r = 0.307$ ,  $St_p = 3.2$ . (a) Snapshots from experiments corresponding to three different time instances:  $t_0^*$ ,  $t_1^*$  and  $t_2^*$ . (b) Time evolution of the  $x$  and  $z$  particle positions. (c) Three-dimensional spatial reconstruction of the particle's trajectory based on shadowgraphy measurements. (d) Time evolution of the vertical position  $y$  of both the particle (P) and the vortex ring (VR). (e) Time derivative of the particle trajectory. (f) The trajectory in terms of radial and vertical position of the particle. In (d–f), the times  $t_1^*$  and  $t_2^*$  are marked with diamond and circle symbols, respectively. The square symbol indicates the moment when the particle and the vortex ring are at the same vertical position for the first time. Additionally, the first three instances when the particle is at the same vertical position as the core of the vortex ring are indicated by a square symbol, followed by  $i$  and then  $ii$ .

its core. This phenomenon is illustrated by the transient negative velocity observed in figure 7(e). This is a required condition to qualify the encounter as a strong deviation in this study. At  $t_2^*$ , the particle is back to a vertical trajectory at the terminal rising velocity. Depending on the properties of the vortex rings and the initial position of the particle prior to the encounter, different patterns of strong deviation can be observed, leading to different particle trajectories. However, in all cases, the particle's velocity while encountering the vortex ring becomes momentarily negative. Then, after a certain time ( $< t_2^*$ ), the particle escapes and returns to its rising trajectory. The condition for qualifying the regime as a strong deviation is defined as

$$\exists t^* \in [0, t_2^*] : U_{p,y}(t^*) < 0 \quad \wedge \quad \exists t^* \in [t_{ce}^*, t_2^*] : \left| \frac{y_p(t^*) - y_{VR}(t^*)}{D_{VR}} \right| > 0.5. \quad (4.2)$$

Here, the threshold 0.5 corresponds to a vertical displacement (in the vortex ring reference frame) beyond which the particle is still encountering the vortical structure.

### 4.3. Capture

When the encounter between the vortex ring and the particle leads to entrainment of the particle by the ring, the regime is called capture. Figure 8 presents an overview of this regime. As observed for the strong deviation regime, at  $t_1^*$ , the particle starts interacting with the vortex, and its rising velocity decreases (see figure 8c,d). Again, the particle deviates from its initial trajectory after  $t_1^*$  (see figure 8e) to reach the outer edge of the vortex located at  $0.5D_{VR} + a$  after approximately one inertial time  $\tau_i$  (square symbol

in figure 8f). Up to this point, the particle behaviour is similar to that of the strong deviation regime. However, the particle is then captured by the vortex ring, displaying a quasi-circular motion near its core. The maximum descending velocity is reached when the particle is at the vortex ring level on the inner part (see *i* in figure 8d–f). On the other hand, the maximum ascending velocity is reached when the particle is axially aligned with the vortex ring on the outer part (see *ii* in figure 8d–f). Furthermore, in the visualisation window shown here, both the radial extension of the quasi-circular trajectory of the particle and the magnitude of its velocity during that motion barely change. This is also evidenced by the particle position projected in the  $xz$  plane in figure 8(b), where the particle stays relatively close to the vortex core during the vortex propagation. Eventually, the vortex ring loses its intensity due to viscous effects, and the particle escapes the vortex structure. However, this long-term step is not in the scope of the present study. In this way, the condition used here to classify the regime as a capture regime is mathematically expressed as

$$\exists t^* \in [0, t_2^*] : U_{p,y}(t^*) < 0 \quad \wedge \quad \left| \frac{y_p(t^*) - y_{VR}(t^*)}{D_{VR}} \right| < 0.5 \quad \forall t^* \in [t_{ce}^*, t_2^*]. \quad (4.3)$$

#### 4.4. Regime mapping in parameter space

The three specific configurations described earlier represent different interaction regimes that are observed under varying conditions, based on the properties of the generated vortex rings ( $D_{VR}$ ,  $\bar{U}_{VR}$ ) and the initial relative position of the particle. Each experiment is defined by two dimensionless parameters: the Stokes number ( $St_p$ ) and the relative release position ( $R_r$ ). Figure 9 shows a map of the interaction regimes in an ( $St_p$ ,  $R_r$ ) diagram. As the particle released is the same, its terminal rising velocity should always be the same. Taking into account experimental errors, the ascent terminal velocity of the particle, considering all experiments, exhibits a Gaussian-like distribution. Particles whose rising velocity is outside the interdecile range are not considered. Significant variations may be due to a bubble that has adhered to the surface of the particle, or to the initial rotation of the particle, which adds a Magnus effect to it, preventing it from achieving a linear ascent over the available distance. By the end, the experiments removed represent approximately 20 % of the cases. For each experiment represented by a symbol in figure 9, the relative position of the particle and its density are determined *a posteriori*. The particle position is measured when it lies  $1.5D_{VR}$  below the vortex ring, which enables the calculation of  $R_r$ . The particle density  $\rho_p$  is obtained from the terminal velocity measured along the undisturbed trajectory segment prior to the interaction, from which the corresponding Stokes number  $St_p$  is then calculated. The presence of microbubbles, along with minor experimental uncertainties, introduces slight deviations in the terminal velocity compared to the targeted value based on the *a priori* known  $\rho_p$ ; besides that, for each experiment, the vortex ring velocity  $\bar{U}_{VR}$  is calculated for  $t/\tau_i \in [1, 7]$ . This correction explains the small scatter of  $St_p$  values around the three aimed values ( $St_p = 2.4, 3.2, 4.7$ ) reported in table 1.

As expected, when the particle is released beyond a critical radial distance, it is not affected by the vortex ring. This critical distance is observed to be  $R_r \geq 1$ . When the particle is initially at a relative position  $r_{rel}$ , allowing it to enter the vortex's zone of influence, all regimes can be observed. It seems that if the particle initially evolves on the outside of the vortex core, for  $R_r \geq 0.5$ , then simple deviations are observed regardless of the Stokes number. However, particles released on the inner side of the vortex ring can have various types of interaction with it, depending on the Stokes number.



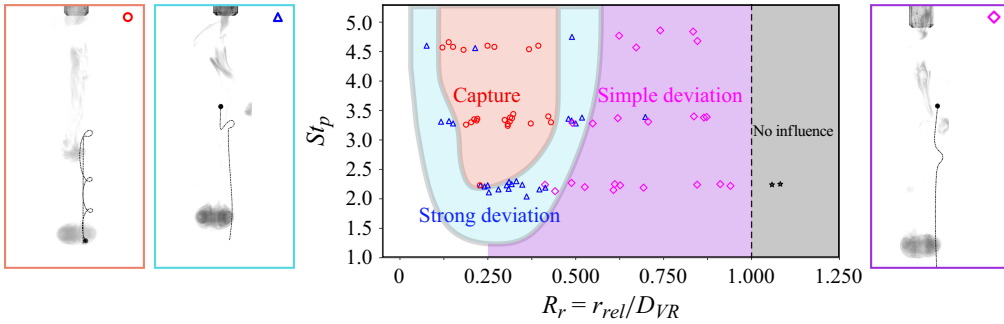


Figure 9. Regime mapping of the interaction between an inertial particle and a vortex ring. Circles represent the capture regime, triangles indicate the strong deviation regime, and the simple deviation regime is marked with diamonds. To make reading easier, the colour of the symbol has been used to colour the background of the areas that contain it: purple for simple deviation, blue for strong deviation, and red for capture. An example of the particle trajectory associated with each regime is shown on the sides of the map, with the respective symbol at the top. The configurations  $(St_p, R_r)$  for each regime are as follows: capture (3.2, 0.307), strong deviation (2.2, 0.229), and simple deviation (2.2, 0.626).

The capture regime is only observed in a narrow region of the diagram (red area in figure 9) for  $R_r \in [0.125, 0.375]$  and for Stokes number beyond 2. In the case of slower vortex rings released from the same position, the observed behaviour was primarily strong deviation. The Stokes number, defined by (2.3), represents the ratio of the characteristic time scales of a particle and the surrounding fluid. Since the particle remains unchanged, its characteristic time scale also remains constant; thus a higher Stokes number indicates a stronger vortex.

Similar results for the capture regime were observed numerically by Fung (2000) on a two-dimensional configuration for which small heavy particles came into contact with a vortex formed by a spiral vorticity sheet. It was observed that the interactions were mainly governed by particle inertia and relative position to the vortex core centre, in agreement with the present observations. However, in the experimental set-up of this study, the inertia of the particles is constant, but the important quantity is the ratio between the inertia of the particle and the inertia of the vortex structure. In the range of parameters of this study, the higher the Reynolds number associated with the vortex ring (or larger  $St_p$ ), the higher the probability of observing a capture. However, further investigation at higher Reynolds numbers would be necessary, as it is expected that at some point, for sufficiently high Reynolds numbers, capture may not be possible. A larger Reynolds number implies a shorter time scale for the vortex ring, which reduces the time available for the particle to respond to the induced flow field, thereby decreasing the probability of capture.

## 5. Numerical simulations

The primary objective of the numerical simulations is to identify the hydrodynamic forces required to identify the interaction regimes observed experimentally. Beyond that, a faithful numerical reproduction of the experimental observations, i.e. a reproduction of the distribution of the regimes in the parameter space, makes it possible to rule on the relative contributions of each of the hydrodynamic forces, and ultimately to address the question of the physical mechanisms of interaction.

## 5.1. Model formulation and method

The direct numerical simulations are performed using the finite-volume open-source solver Basilisk (Popinet 2015, 2024). The vortex ring is simulated in an Eulerian framework, considering incompressible fluid. The mass and momentum conservation equations are written as

$$\nabla \cdot \mathbf{u} = 0, \quad (5.1)$$

$$\frac{\partial \mathbf{u}}{\partial t} + (\mathbf{u} \cdot \nabla) \mathbf{u} = -\frac{\nabla p}{\rho_f} + \nu_f \nabla^2 \mathbf{u}, \quad (5.2)$$

where  $\mathbf{u} = (u, v, w)$  is the three-dimensional velocity,  $\nu_f = \mu_f / \rho_f$  is the kinematic viscosity, and  $p$  is the pressure. A triple-periodic boundary condition in a cubic domain with dimension  $L = 50D_g$  is applied to avoid wall effects. The discrete Navier–Stokes equations are solved using a fourth-order-accurate solver with an upwind advection scheme (van Hooft & Popinet 2022). The spatial discretisation employs adaptive mesh refinement based on a wavelet estimate of the discretisation error in the velocity field (threshold  $10^{-3}$ ). A mesh sensibility test was realised to verify the spatial discretisation convergence (not shown).

The approach chosen by van Hooft & Popinet (2022) has been implemented in this study to generate vortex rings as a torus whose azimuthal section is a Lamb–Oseen vortex (Oseen 1910; Lamb 1932). Therefore, the initial vorticity distribution is

$$\boldsymbol{\omega}(x, y, z) = \oint_{C_1} \frac{\Gamma_{num,0}}{\pi^{3/2} a_{num,0}^3} \exp\left(-\frac{r_c^2}{a_{num,0}^2}\right) d\mathbf{l}, \quad (5.3)$$

where  $\Gamma_{num,0}$  is the vortex circulation,  $a_{num,0}$  is the radius of the vortex core, and the integration contour is  $C_1(x_0, y_0, z_0, \phi \in [0, 2\pi]) = ((D_{VR}/2) \cos(\phi), H_y, (D_{VR}/2) \sin(\phi))$ , with  $H_y$  the initial vertical position of the vortex. The initial vorticity field  $\boldsymbol{\omega}$  is defined as a function of the radial distance to the core centre  $r_c = ((x - x_0)^2 + (z - z_0)^2)^{1/2}$ , and the integration element is  $d\mathbf{l} = \partial C_1 / \partial \phi$ . The vorticity field is resolved using a fourth-order-accurate Gauss–Legendre quadrature rule, and consists of solving a three-dimensional Poisson problem  $\nabla^2 \boldsymbol{\Psi} = -\boldsymbol{\omega}$ , with  $\boldsymbol{\Psi}$  the stream-function vector. Finally, the flow field is given by  $\mathbf{u} = \nabla \times \boldsymbol{\Psi}$ . Once the vortex ring is initialised, it propagates in a self-induced way, as expected. The parameters of the Lamb–Oseen model have been chosen to reproduce the experimental results as faithfully as possible. The sizes of the core and diameter of the vortex ring are directly estimated from the experimental measurements. Finally, the circulation is adjusted in order to match the propagation velocity measured experimentally.

The particle dynamics is modelled using a Maxey–Riley approach (Maxey & Riley 1983; Gatignol 1983). Specifically, a linear superposition of independent hydrodynamical forces acting on the particle is considered here. As justified by the analysis of experimental measurements, the vortex ring–particle interaction is assumed to be a one-way coupling. Following Mathai *et al.* (2020), the Lagrangian equation for the dynamics of a single particle is given by

$$V_p \rho_p \frac{d\mathbf{U}_p}{dt} = \mathbf{F}_B + \mathbf{F}_L + \mathbf{F}_D + \mathbf{F}_{AM} + \mathbf{F}_{PG}, \quad (5.4)$$

where  $\mathbf{U}_p$  is the particle's velocity,  $V_p = d_p^3 \pi / 6$  is its volume, and  $m_p = V_p \rho_p$  is its mass. These particle parameters are defined in order to reproduce the one from the experiment. Nevertheless, it should be noted that the simulation treats the particle as point-like.

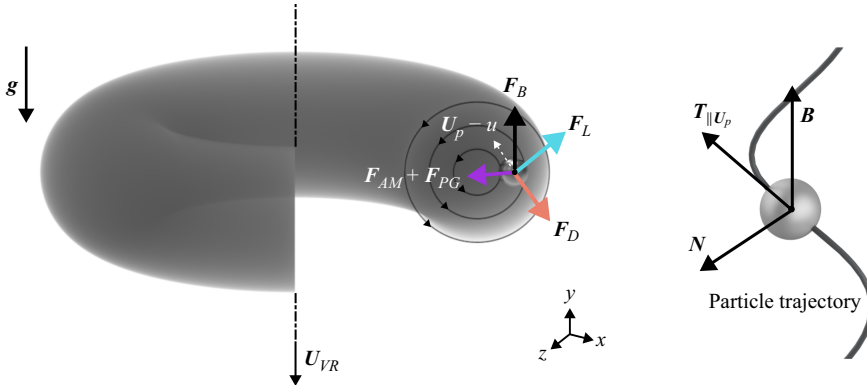


Figure 10. Forces acting on an inertial particle in the vicinity of a vortex ring, and definition of the Frenet–Serret coordinate system, where  $F_B$  is the buoyancy force,  $F_D$  is the drag force, opposite to the particle relative velocity ( $U_p - u$ ),  $F_L$  is the lift force in the plane orthogonal to the particle relative velocity, and  $F_{AM} + F_{PG}$  is the inertial force that takes into account the added mass and pressure gradient forces. Vectors sizes are arbitrary. The unit vector  $T$  is aligned with the particle trajectory, unit vector  $N$  points to the trajectory curvature centre, and  $B = T \times N$ .

Consequently, the particle has only three translational degrees of freedom, there is no feedback on the surrounding fluid, and all forces are modelled as point forces acting at its centre of gravity. On the right-hand side, force contributions are the buoyancy force  $F_B$ , the shear-induced lift  $F_L$ , the drag  $F_D$ , the added mass  $F_{AM}$ , and the pressure gradient  $F_{PG}$ , defined as follows:

$$F_B = V_p(\rho_p - \rho_f)g, \quad (5.5)$$

$$F_L = -C_L \rho_f V_p (U_p - u) \times (\nabla \times u), \quad (5.6)$$

$$F_D = -C_D \frac{\pi d_p^2}{8} \rho_f |U_p - u| (U_p - u), \quad (5.7)$$

$$F_{AM} = C_{AM} \rho_f V_p \left( \frac{Du}{Dt} - \frac{dU_p}{dt} \right), \quad (5.8)$$

$$F_{PG} = V_p \rho_f \frac{Du}{Dt}. \quad (5.9)$$

In these equations,  $C_L$ ,  $C_D$  and  $C_{AM}$  are the lift, drag and added mass coefficients, respectively, and  $g$  is the acceleration due to gravity. For a sphere, the added mass coefficient is  $C_{AM} = 1/2$  (Auton, Hunt & Prud’Homme 1988). The drag coefficient  $C_D$  is given by Schiller & Naumann (1935) as  $C_D = 24/Re_p(1 + 0.15 Re_p^{0.687})$ , with  $Re_p$  the particle Reynolds number defined as  $Re_p = \rho_f U_p d_p / \mu_f$ . Assume that the Auton lift for a momentum flux far from the particle in shear flow,  $C_L$ , is 0.5.

Figure 10 shows a graphical representation of the forces acting on the particle’s dynamics in the vicinity of a vortex ring. The drag force acts in the opposite direction to the relative velocity  $U_p - u$  (Zimmermann *et al.* 2011). The lift force belongs to the plane orthogonal to the direction of the relative velocity (Auton *et al.* 1988). The buoyancy force is, by definition, aligned with gravity and therefore the vertical axis. The added mass and pressure gradient forces are present as a net term that will be referred to as inertial force hereafter. Particle dynamics (5.4) is calculated using a trilinear interpolation of the fluid

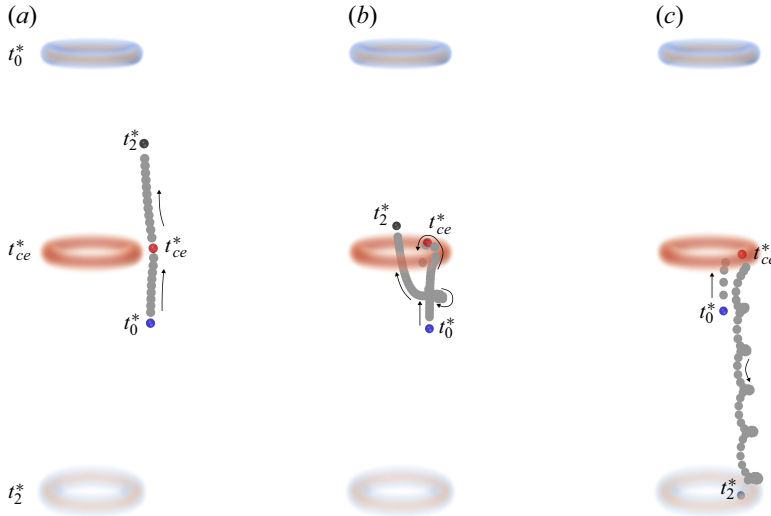


Figure 11. Volumetric rendering of the  $\lambda_2$  criterion for vortex identification and particle trajectories (grey circles) under different kinematics regimes. Trajectories are shown in between  $t_0^*$  and  $t_2^*$  for (a) a simple deviation, (b) a strong deviation, and (c) a capture regime.

velocity and its spatial derivatives. This interpolation uses the values from the surrounding cell centres of the adaptive mesh, which is also used for fluid resolution. The particle's motion is simulated over time using an explicit, first-order scheme. To analyse the forces acting on the particle, a specific Frenet–Serret coordinate system  $(\mathbf{T}, \mathbf{N}, \mathbf{B})$  that follows its trajectory is defined. In this system,  $\mathbf{T}$  (tangent) is aligned with the particle's velocity,  $\mathbf{N}$  (normal) points towards the centre of the trajectory's curvature, and  $\mathbf{B}$  (binormal) is perpendicular to both  $\mathbf{T}$  and  $\mathbf{N}$  (where  $\mathbf{B} = \mathbf{T} \times \mathbf{N}$ ). The projection of the forces into this coordinate system is illustrated in figure 10.

## 5.2. Comparison with experimental results

Figure 11 shows an example of each of the three regimes obtained numerically. In this figure, the particle trajectory is shown between  $t_0^*$  and  $t_2^*$ , as first introduced in § 4.1, and the vortex ring is identified by a volumetric rendering of the  $\lambda_2$  criterion at  $t_0^*$ ,  $t_{ce}^*$  and  $t_2^*$ . The three previously defined regimes of simple deviation, strong deviation and capture are unambiguously identifiable from left to right.

Similar to the experimental study, the numerical observations are represented in an  $(St_p, R_r)$  diagram. Each symbol in figure 12 corresponds to a numerical simulation based on a pair of initialisation parameters  $(St_p, R_r)$ . The background colours indicate the regions defined by the experimental data shown in figure 9. With only slight differences, the overall regime map obtained from numerical simulations matches very well the experimental one, given the simple one-way coupling point-like method used for the particle interaction. The differences are mainly observed near the boundaries between the regimes, which was to be expected since the contours were drawn arbitrarily, without any physical support for the delimitations. Interestingly, the capture zone extends towards the lower left corner of the map ( $St_p \leq 2.5$  and  $R_r \leq 0.25$ ). These initialisation configurations were not experimentally feasible.

This regime mapping was obtained numerically without taking into account the lift force  $F_L$ . Several values of the lift coefficient were examined, including the reference value  $C_L = 0.5$ , over the range  $C_L \in [0.025, 0.5]$  for all cases tested. However, for this particular

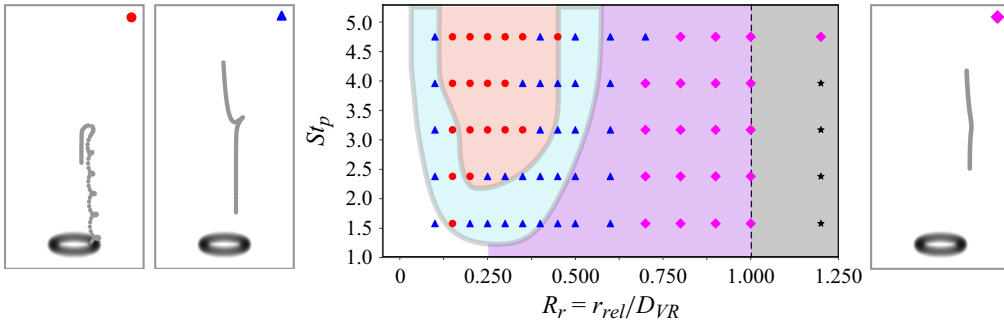


Figure 12. Mapping of the regimes in an  $(St_p, R_r)$  diagram. Numerical results are shown using filled symbols. The background coloured area is associated with the experimental regime map for comparison (see figure 9). Red circles are captures, blue triangles are strong deviations, and magenta diamonds are simple deviations.

configuration, the literature does not provide a universally applicable lift coefficient across all flow conditions (Saffman 1965; Auton *et al.* 1988; Lee & Balachandar 2010). It could even be possible that the lift coefficient should vary in time and space. Finally, and as (i) the regimes were matching the localisation of the ones obtained experimentally and (ii) the trajectories of numerical and experimental particles were very similar without taking into account the lift force (see figure 12), for simplicity, this force was discarded.

### 5.3. Governing forces in the simple deviation regime

Figure 13(a) shows a typical comparison of the trajectories obtained numerically and experimentally for a simple deviation regime. The two trajectories are very close to each other. To better understand the successive stages of the simple deviation process, figure 13(b) shows the temporal evolution of the magnitude of forces acting on the particle. The force  $F_p$ , represented by the black curve, is the magnitude of the total force acting on the particle. All forces are made non-dimensional with  $F_B$ , the magnitude of the buoyancy force. Figure 13(c) represents the forces applied to the particle at given moments  $t_1^*$ ,  $t_{ce}^*$ , and an arbitrary post-encounter time  $t_{pe}^*$ . Note that the relative amplitudes and directions of the vectors are to scale.

Before the particle's trajectory begins to be affected by the vortex ring (i.e. for  $t^* < t_1^*$ ), the particle rises in the tank at its terminal velocity resulting from the balance between buoyancy and drag (see figure 13b). From  $t_1^*$  onwards, the particle's trajectory deviates from its initial vertical ascension due to the inertial force  $F_{AM} + F_{PG}$  that pushes the particle out of the vortex (see figure 13c). At  $t_{ce}^*$ , the particle and the core of the vortex ring are at the same altitude  $y$ . As shown in figure 13(c), the inertial force becomes the leading one, and the local pressure minimum at the vortex core attracts the particle towards the axis of symmetry. Nevertheless, the force is not strong enough to carry the particle along with the vortex ring, and the particle eventually escapes from the vortex structure. The inertial force diminishes in favour of drag–buoyancy equilibrium that is recovered from  $t^* \approx t_{pe}^*$ , and inertial forces vanish at  $t_2^*$ .

### 5.4. Governing forces in the capture regime

A comparison of the trajectories obtained from an experiment and the numerical simulation for a capture regime is shown in figure 14(a), while figure 14(b) presents the time evolution of the forces acting on the particle.

The particle trajectories observed in the experiment and the corresponding numerical simulation display a similar trend – specifically, a periodic trajectory centred around the

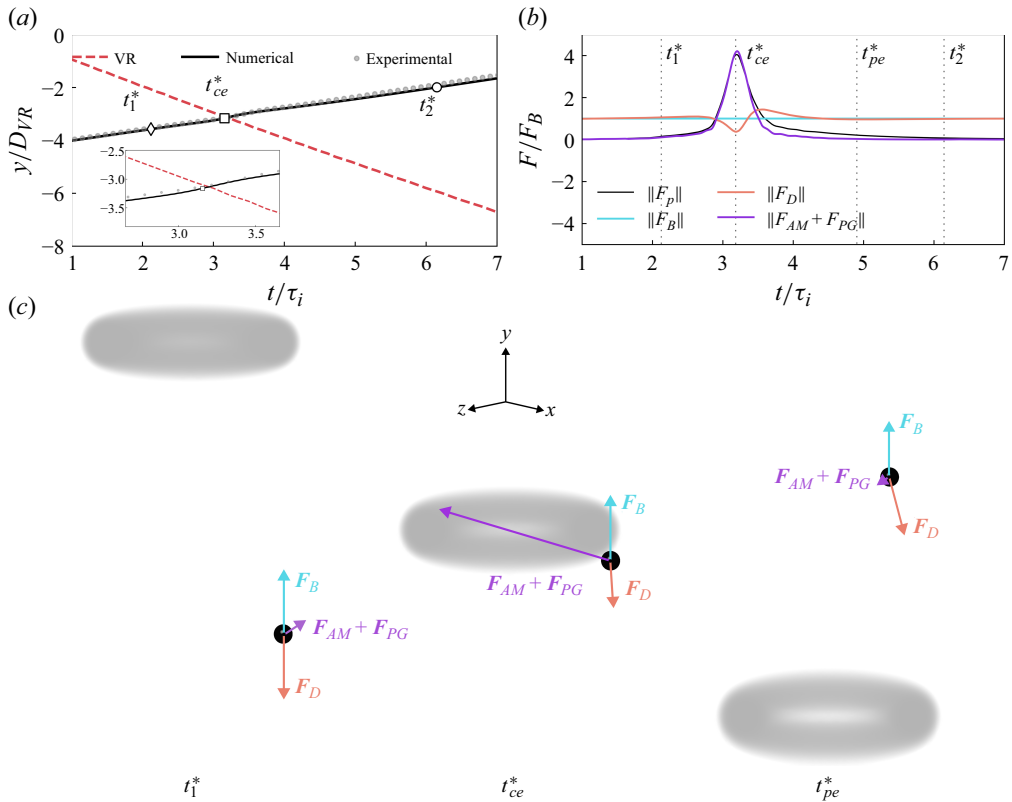


Figure 13. Experimental comparison and particle dynamics in the simple deviation regime ( $R_r = 0.756$ ,  $St_p = 3.17$ ). (a) Time evolution of the particle's vertical position, showing both experimental data (grey points) and numerical results (solid black line), alongside the vertical position of the vortex ring (dashed red line). (b) Time evolution of the magnitudes of the forces acting on the particle, normalised by the magnitude of the buoyancy force  $F_B$ . Here,  $F_p$  (black line) represents the total force, while  $F_D$  and  $F_{AM} + F_{PG}$  denote the drag and inertia forces, respectively. (c) Representation of these forces at three different times:  $t_1^*$ ,  $t_{ce}^*$  and  $t_{pe}^*$ . The magnitude of the forces is represented to scale. The vortex ring is illustrated through a volumetric rendering using the  $\lambda_2$  criterion.

core of the vortex ring. This is illustrated by the oscillations of the solid black line along the red dashed line in [figure 14\(a\)](#). However, the simulation shows an underestimated amplitude and an overestimated frequency for the periodic trajectory, which may be attributed to the point-like nature of the particles. It is important to note that despite the possible significance of finite-size effects in this configuration, the point-like particle approximation can reproduce the experimental results. This observation is consistent with findings from [Angriman \*et al.\* \(2022\)](#) and [Battista, Chibbaro & Gualtieri \(2025\)](#), which indicate that (5.4) remains valid even beyond its theoretical limits across different flow regimes.

Three primary stages may be identified in the particle's dynamics (see [figure 14\(b\)](#)). As long as the particle is away from the vortex ring, the buoyancy and drag forces balance each other leading to a particle rising at constant terminal velocity. Then the drag force dramatically increases after  $t/\tau_i = 3$ , and the vortex ring suddenly slows the particle down. At the same time, the added mass and pressure gradient forces, both of which involve the flow velocity gradient, develop. Subsequently, for  $t/\tau_i > 3.5$ , the drag, proportional to the velocity difference between the particle and the flow, diminishes, indicating that



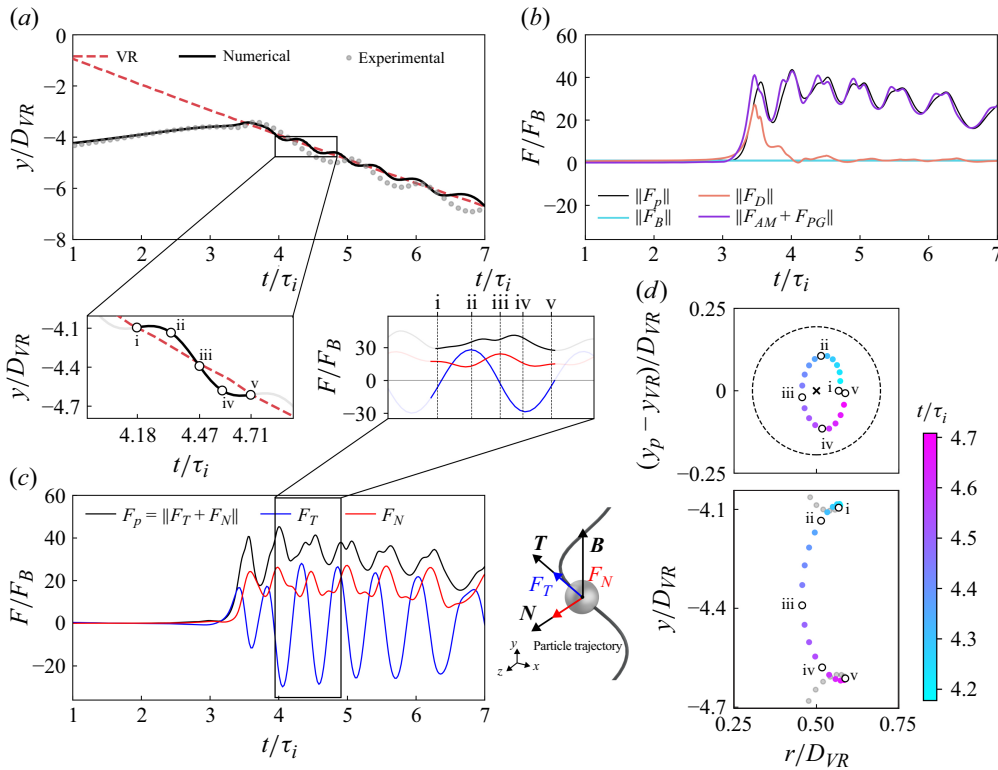


Figure 14. Experimental comparison and particle dynamics in the capture regime ( $R_r = 0.261$ ,  $St_p = 3.17$ ). (a) Time evolution of the particle's vertical position, with experimental data represented by grey points, and numerical data by a solid black line. The vertical position of the vortex ring is indicated by a red dashed line. (b) Time evolution of the magnitudes of the forces acting on the particle. (c) The projection of  $F_p$  along the particle trajectory,  $F_T$ , and in the plane orthogonal to it,  $F_N$ . The forces in (b) and (c) are normalised by the magnitude of the buoyancy force  $F_B$ . (d) The particle trajectory in the vortex ring reference frame (top) and in the laboratory reference frame (bottom) for an arbitrary quasi-circular trajectory around the vortex core during the vortex ring and particle interaction. Specific moments during this trajectory are identified by the symbols from i to v in (d), and have a correspondence in insets of (a) and (c).

the particle's velocity aligns with the local flow velocity. The inertial force becomes the dominant one acting on the particle and is consequently responsible for the specific capture trajectory.

Figure 14(c) shows the total force applied to the particle projected along the trajectory,  $F_T$ , and in the plane orthogonal to it,  $F_N$ . The curvilinear trajectory is associated with the fact that  $F_N$  is non-zero. The oscillations of  $F_T$  and  $F_N$  are the result of variations in the pressure gradient along the trajectory of the particle, and are discussed in the following.

The trajectory of the particle in figure 14(d) is shown for a complete radial trajectory around the core of the vortex ring in both the vortex ring (top) and the laboratory reference frame (bottom). The gap between two consecutive points represents a fixed time interval. The components of the total force acting on the particle as it traverses the trajectory are presented in the inset of figure 14(c). First, note that the trajectory of the particle in the reference frame of the travelling vortex is elliptical. This elliptical trajectory must be linked to fluctuations in the  $F_N$  component of the force acting on the particle.

Regarding the component of the force aligned with the trajectory,  $F_T$ , it exhibits an oscillation period during the traversal of the complete radial trajectory. The force is

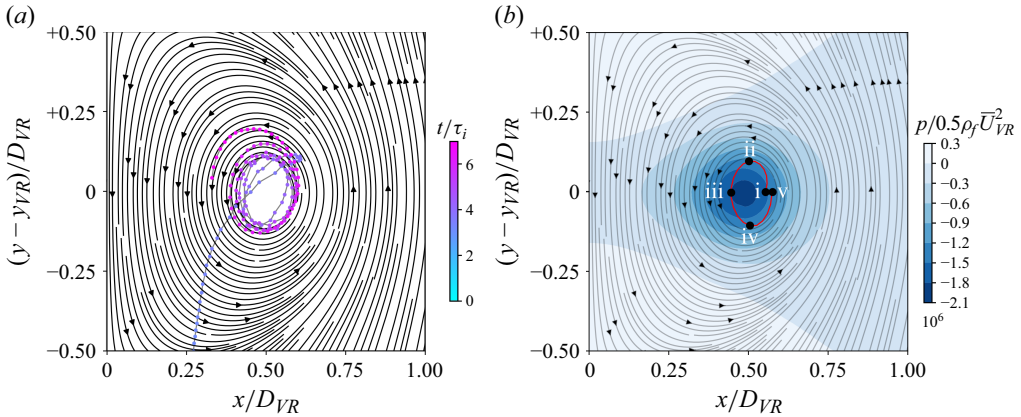


Figure 15. Particle trajectory in the capture regime ( $R_r = 0.261$ ,  $St_p = 3.17$ ). (a) Particle trajectory coloured by time and velocity streamlines (black lines). (b) Portion of the particle's trajectory identical to that detailed in figure 14(d) (red), along with the pressure field (colour) and the velocity streamlines (black lines). The data are plotted in the vortex ring reference frame.

positive, thus the particle accelerates along its trajectory when it passes above the core of the vortex ring (between i and iii), then it becomes negative (i.e. deceleration of the particle along its trajectory) when the particle passes below the centre of rotation (between iii and v). At stages i or v of the highlighted trajectory, the particle rises in the vortex ring reference frame, but is almost immobile in the laboratory frame, as illustrated by the nearly horizontal parts of the trajectory  $y(t)$  between i and ii, and between iv and v in the inset of figure 14(a). The maximum velocity of the particle along its trajectory, on the other hand, is reached at stage iii.

As a complement, figure 15 shows the particle's trajectory in the moving reference frame along with the velocity streamlines (figure 15a) and the pressure field (figure 15b). The configuration shown corresponds to that of figure 14, and the Reynolds number is  $Re = 2400$  (see table 1). According to figure 4, the compactness of the vortex ring is therefore  $2a/D_g \approx 0.39$ , or equivalently,  $2a/D_{VR} \approx 0.23$ . Although the particle does not strictly follow a streamline due to the density ratio  $\rho_p/\rho_f$ , it seems that the particle orbits around the vortex core very close to its spatial extension  $2a/D_{VR}$ . As the vortex core centre is not aligned with the pressure field, the particle crosses several isobars along its trajectory (see figure 15b). The tangents to the trajectory and the isobar of highest magnitude coincide at point iii. This point naturally corresponds to a force that vanishes along the trajectory, i.e.  $F_T = 0$ , and a maximum of  $F_N$  is measured at this location (see inset in figure 14c). Similarly, the orientation of the isobars relative to the trajectory at points ii and iv is associated with the extrema of the  $F_T$  component of the force and minima of  $F_N$ . Finally, following several periodic quasi-circular trajectories (see figure 14c), the normal component of the total force,  $F_N$ , exhibits an oscillation frequency twice as high as that of the tangential component,  $F_T$ . The oscillation period of the tangential force corresponds to that of the particle's quasi-circular trajectory around the core of the vortex ring, i.e.  $\tau_i = D_{VR}/U_{VR}$ , the inertial time scale of the vortex ring.

### 5.5. Governing forces in the strong deviation regime

The strong deviation can be seen as an intermediate regime between simple deviation and capture. The trajectory of the vortex ring is shown in dashed red in figure 16(a), whereas the trajectory of the particle is shown in solid black. Shortly after  $t/\tau_i = 3$ ,

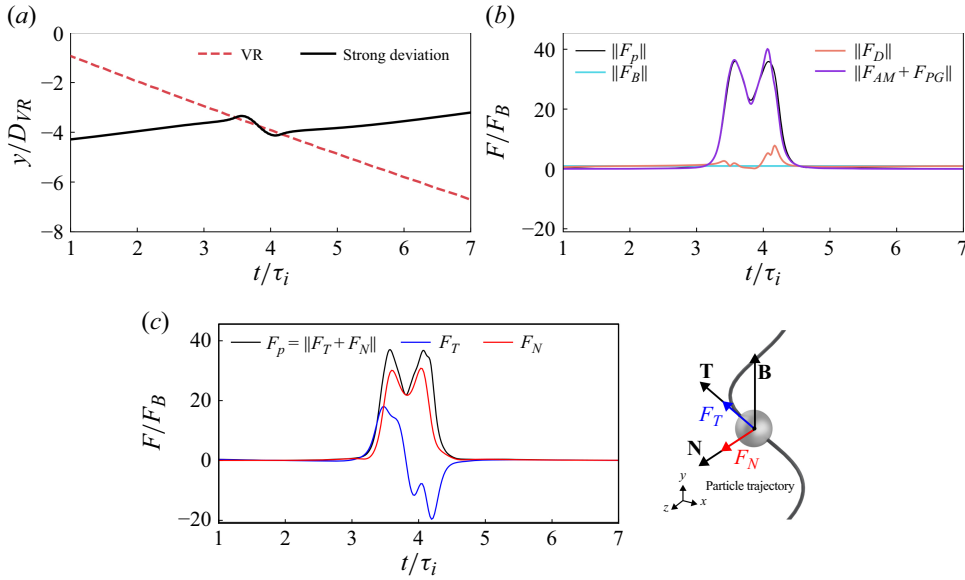


Figure 16. The vertical position of the particle and the forces acting on it in the strong deviation regime ( $R_r = 0.600$ ,  $St_p = 3.17$ ). (a) Time evolution of the particle vertical position (black line) along with the vortex ring vertical position (dashed red line). (b) Time evolution of the magnitude of the forces acting on the particle, where  $F_p$  represents the total force,  $F_B$  the buoyancy force,  $F_D$  the drag force, and  $F_{AM} + F_{PG}$  the inertia force. (c) Time evolution of the total force acting on the particle,  $F_p$ , and its projection along the trajectory  $F_T$  and orthogonal to it  $F_N$ . The forces are normalised by the magnitude of the buoyancy force  $F_B$ .

the particle reaches the vortex structure vertical level. It then circles the vortex ring's core for approximately one inertial time scale  $\tau_i$  before escaping and heading back to its original trajectory shortly after  $t/\tau_i = 4$ .

The time evolutions of the forces acting on the particle are presented in figure 16(b). Similar to the capture regime, the inertial force is primarily responsible for the initial trapping of the particle. Regarding the projection of the total force along the trajectory and perpendicularly to it (as shown in figure 16c), the quasi-circular trajectory of the particle can be distinguished by the substantial contribution of the force  $F_N$  developing in the plane orthogonal to the trajectory. The particle then experiences a sharp slowdown just before  $t/\tau_i = 4$  (negative peak of  $F_T$ , and appearance of a peak of drag  $F_D$ ). Finally, the loss of inertia of the particle, combined with the weakness of the vortex ring, leads to the fact that nothing can counteract the buoyancy force any more. This causes the  $F_N$  component of the force to revert to zero, returning the particle to its original ascending trajectory.

## 6. Conclusions

The interaction between a vortex ring and a single inertial particle was investigated using an experimental and numerical approach. For the range of parameters under the scope of this study, experimental observation reveals that the interaction between a particle and the vortex ring falls into three regimes: simple deviation, strong deviation and capture. The regime is referred to as simple deviation when the buoyant particle, although experiencing some velocity variations in the vortex ring vicinity, maintains its ascending motion along the whole trajectory. The capture regime occurs when the particle is trapped inside the vortex structure on a time scale greater than the inertial time scale of the vortex. Strong deviation is an intermediate regime for which the particle is initially attracted into the

structure, but eventually escapes to regain its own ascending dynamics over a time shorter than the vortex's inertial characteristic time.

These experimental observations could be reproduced with a numerical point-like model of the particle using a one-way coupling approach. This simple model can reproduce the regime map in an  $(St_p, R_r)$  diagram, and allows for the investigation of each force's influence on the particle (5.4) individually. The principal forces responsible for the mechanisms involved in the particle dynamics in the vortex ring–particle interaction can then be identified. It turns out that only three forces are necessary to reproduce the distribution of regimes in the parameter diagram, namely buoyancy, drag, and inertial forces consisting of added mass effects and pressure gradient. The initial ascension at a terminal rising velocity results from an equilibrium between buoyancy and drag. Then the inertial force appears in the vicinity of the vortex ring and leads to one of the three regimes, depending on the controlling parameters. When the relative position of the particle  $R_r$  is higher than the vortex ring radius, the particle only experiences a simple deviation, regardless of the Stokes number. On the other hand, for  $R_r < 0.5$ , both the relative position and the Stokes number matter, leading to either strong deviations or captures. The codes used in this study are available in Basilisk sandbox (de Aquino 2025).

This study provides new insights into the understanding of particle transport and mixing by a coherent structure. According to the results, adjusting the parameters of the regime distribution diagram may allow for some degree of control over these processes. To achieve this goal, it would be beneficial to extend this diagram. More importantly, it would be necessary to vary the Stokes number according to the particle's size and density to confirm the universality of the results. Finally, a complementary investigation using a resolved particle and a two-way coupling model would provide a more accurate determination of the forces involved, especially the evaluation of the forces induced by the rotation of the particle.

**Acknowledgements.** The authors would especially like to thank L. Lacaze and P. Brancher, who contributed to the supervision of the internship of N.S.. Fruitful conversations with them enabled us to characterise vortex rings more precisely, and in general, contributed to the investigation of the interaction processes discussed in this work. The authors also gratefully acknowledge N. Reboucier, who performed the first numerical tests and debugging during his internship.

**Funding.** This research received no specific grant from any funding agency, commercial or not-for-profit sectors.

**Declaration of interests.** The authors report no conflict of interest.

## REFERENCES

- ALBAGNAC, J. & ANNE-ARCHARD, D. 2024 Starting jets in non-Newtonian viscoelastic fluids: on vortex ring generation and behavior. *Exp. Fluids* **65**, 164.
- AN, D., WARNING, A., YANCEY, K.G., CHANG, C.-T., KERN, V.R., DATTA, A.K., STEEN, P.H., LUO, D. & MA, M. 2016 Mass production of shaped particles through vortex ring freezing. *Nat. Commun.* **7** (1), 12401.
- ANGRIMAN, S.D., FERRAN, A., ZAPATA, F., COBELLI, P.J., OBLIGADO, M. & MININNI, P.D. 2022 Clustering in laboratory and numerical turbulent swirling flows. *J. Fluid Mech.* **948**, A30.
- DE AQUINO, G.S. 2025 Code repository. Available at <https://basilisk.fr/sandbox/gaquino/>.
- ARVIDSSON, P.M., KOVÁCS, S.J., TÖGER, J., BORGQUIST, R., HEIBERG, E., CARLSSON, M. & ARHEDEN, H. 2016 Vortex ring behavior provides the epigenetic blueprint for the human heart. *Sci. Rep.-UK* **6** (1), 22021.
- AUTON, T.R., HUNT, J.C.R. & PRUD'HOMME, M. 1988 The force exerted on a body in inviscid unsteady non-uniform rotational flow. *J. Fluid Mech.* **197**, 241–257.
- BATTISTA, F., CHIBBARO, S. & GUALTIERI, P. 2025 Assessment of the point-wise approach for the turbulent settling of finite-size particles. *Intl J. Multiphase Flow* **190**, 105276.

- BENTATA, O., ANNE-ARCHARD, D. & BRANCHER, P. 2018 Experimental study of low inertia vortex rings in shear-thinning fluids. *Phys. Fluids* **30** (11), 113103.
- BISWAS, S. & GOVARDHAN, R.N. 2022 Interaction of a rigid buoyant sphere and a deforming bubble with a vortex ring: the role of deformability. *Phys. Rev. Fluids* **7** (9), 094302.
- BISWAS, S. & GOVARDHAN, R.N. 2025 Interaction of a vortex ring with a buoyant spherical particle: effects of particle size on vorticity dynamics and particle dynamics. *J. Fluid Mech.* **1015**, A24.
- BOUREMEL, Y. & DUCCI, A. 2017 Scalar mixing and strain dynamics methodologies for PIV/LIF measurements of vortex ring flows. *Phys. Fluids* **29** (1), 013602.
- BRANDT, L. & COLETTI, F. 2022 Particle-laden turbulence: progress and perspectives. *Annu. Rev. Fluid Mech.* **54** (1), 159–189.
- CALZAVARINI, E., VOLK, R., BOURGOIN, M., LÉVÊQUE, E., PINTON, J.-F. & TOSCHI, F. 2009 Acceleration statistics of finite-sized particles in turbulent flow: the role of Faxén forces. *J. Fluid Mech.* **630**, 179–189.
- DABIRI, J.O. 2009 Optimal vortex formation as a unifying principle in biological propulsion. *Annu. Rev. Fluid Mech.* **41**, 17–33.
- DIDDEN, N. 1979 On the formation of vortex rings: rolling-up and production of circulation. *Z. Angew. Math. Phys.* **30** (1), 101–116.
- DINTRANS, B., BRANDENBURG, A., NORDLUND, Å. & STEIN, R.F. 2005 Spectrum and amplitudes of internal gravity waves excited by penetrative convection in solar-type stars. *Astron. Astrophys.* **438** (1), 365–376.
- ERN, P., RISSO, F., FABRE, D. & MAGNAUDET, J. 2012 Wake-induced oscillatory paths of bodies freely rising or falling in fluids. *Annu. Rev. Fluid Mech.* **44** (1), 97–121.
- FERNANDES, P.C., RISSO, F., ERN, P. & MAGNAUDET, J. 2007 Oscillatory motion and wake instability of freely rising axisymmetric bodies. *J. Fluid Mech.* **573**, 479–502.
- FOURAS, A. & SORIA, J. 1998 Accuracy of out-of-plane vorticity measurements derived from in-plane velocity field data. *Exp. Fluids* **25**, 409–430.
- FUNG, J.C.H. 2000 Residence time of inertial particles in a vortex. *J. Geophys. Res.: Oceans* **105** (C6), 14261–14272.
- GATIGNOL, R. 1983 The Faxén formulæ for a rigid particle in an unsteady non-uniform Stokes flow. *J. Méc. Théor. Appl.* **1**, 143–160.
- GHARIB, M., RAMBOD, E. & SHARIFF, K. 1998 A universal time scale for vortex ring formation. *J. Fluid Mech.* **360**, 121–140.
- GRIMBLE, T.A., AGARWAL, A. & JUNIPER, M.P. 2017 Local linear stability analysis of cyclone separators. *J. Fluid Mech.* **816**, 507–538.
- GROSSHANS, H., BISSINGER, C., CALERO, M. & PAPALEXANDRIS, M.V. 2021 The effect of electrostatic charges on particle-laden duct flows. *J. Fluid Mech.* **909**, A21.
- HINTZE, J.L. & NELSON, R.D. 1998 Violin plots: a box plot–density trace synergism. *Am. Statistician* **52** (2), 181–184.
- HOMANN, H. & BEC, J. 2010 Finite-size effects in the dynamics of neutrally buoyant particles in turbulent flow. *J. Fluid Mech.* **651**, 81–91.
- VAN HOOFT, J.A. & POPINET, S. 2022 A fourth-order accurate adaptive solver for incompressible flow problems. *J. Comput. Phys.* **462**, 111251.
- JHA, N.K. & GOVARDHAN, R.N. 2015 Interaction of a vortex ring with a single bubble: bubble and vorticity dynamics. *J. Fluid Mech.* **773**, 460–497.
- LAMB, H. 1932 *Hydrodynamics*. Cambridge University Press.
- LE DIZÈS, S. & VERGA, A. 2002 Viscous interactions of two co-rotating vortices before merging. *J. Fluid Mech.* **467**, 389–410.
- LEE, H. & BALACHANDAR, S. 2010 Drag and lift forces on a spherical particle moving on a wall in a shear flow at finite  $Re$ . *J. Fluid Mech.* **657**, 89–125.
- LINDEN, P.F. & TURNER, J.S. 2004 ‘Optimal’ vortex rings and aquatic propulsion mechanisms. *Proc. R. Soc. Lond. B: Biol. Sci.* **271** (1539), 647–653.
- MARTÍNEZ-BAZÁN, C. 2015 About bubbles and vortex rings. *J. Fluid Mech.* **780**, 1–4.
- MATHAI, V., LOHSE, D. & SUN, C. 2020 Bubbly and buoyant particle-laden turbulent flows. *Annu. Rev. Condens. Matt. Phys.* **11** (1), 529–559.
- MATHAI, V., NEUT, M.W.M., VAN DER POEL, E.P. & SUN, C. 2016 Translational and rotational dynamics of a large buoyant sphere in turbulence. *Exp. Fluids* **57**, 51.
- MATSUZAWA, T., MITCHELL, N.P., PERRARD, S. & IRVINE, W.T.M. 2023 Creation of an isolated turbulent blob fed by vortex rings. *Nat. Phys.* **19** (8), 1193–1200.
- MAXEY, M.R. & RILEY, J.J. 1983 Equation of motion for a small rigid sphere in a nonuniform flow. *Phys. Fluids* **26** (4), 883–889.

- MAXWORTHY, T. 1972 The structure and stability of vortex rings. *J. Fluid Mech.* **51** (1), 15–32.
- MAXWORTHY, T. 1977 Some experimental studies of vortex rings. *J. Fluid Mech.* **81** (3), 465–495.
- McKEOWN, R., OSTILLA-MÓNICO, R., PUMIR, A., BRENNER, M.P. & RUBINSTEIN, S.M. 2020 Turbulence generation through an iterative cascade of the elliptical instability. *Sci. Adv.* **6** (9), eaaz2717.
- MOUALLEM, J., DARYAN, H., WAWRYK, J., PAN, Z. & HICKEY, J.-P. 2021 Targeted particle delivery via vortex ring reconnection. *Phys. Fluids* **33** (10), 103305.
- NEAU, H., PIGOU, M., FEDE, P., ANSART, R., BAUDRY, C., MÉRIGOUX, N., LAVIÉVILLE, J., FOURNIER, Y., RENON, N. & SIMONIN, O. 2020 Massively parallel numerical simulation using up to 36 000 CPU cores of an industrial-scale polydispersed reactive pressurized fluidized bed with a mesh of one billion cells. *Powder Technol.* **366**, 906–924.
- OLSTHOORN, J. & DALZIEL, S.B. 2018 Vortex-ring-induced stratified mixing: mixing model. *J. Fluid Mech.* **837**, 129–146.
- OSEEN, C.W. 1910 Stokes’ formula and a related theorem in hydrodynamics. *Arkiv. Mat. Astron. Fysik* **6** (20).
- PINAUD, J., ALBAGNAC, J., CAZIN, S., RIDA, Z., ANNE-ARCHARD, D. & BRANCHER, P. 2021 Three-dimensional measurements of an inclined vortex ring interacting with a density stratification. *Phys. Rev. Fluids* **6**, 104701.
- POPINET, S. 2015 A quadtree-adaptive multigrid solver for the Serre–Green–Naghdi equations. *J. Comput. Phys.* **302**, 336–358.
- POPINET, S. 2024 Basilisk. Available at <http://basilisk.fr>.
- PULVIRENTI, F., SCOLLO, S., FERLITO, C. & SCHWANDNER, F.M. 2023 Dynamics of volcanic vortex rings. *Sci. Rep.-UK* **13** (1), 2369.
- QI, Y., TAN, S., CORBITT, N., URBANIK, C., SALIBINDLA, A.K.R. & NI, R. 2022 Fragmentation in turbulence by small eddies. *Nat. Commun.* **13** (1), 469.
- ROSSI, E., BAGHERI, G., BECKETT, F. & BONADONNA, C. 2021 The fate of volcanic ash: premature or delayed sedimentation? *Nat. Commun.* **12** (1), 1303.
- SAFFMAN, P.G. 1965 The lift on a small sphere in a slow shear flow. *J. Fluid Mech.* **22** (2), 385–400.
- SAFFMAN, P.G. 1970 The velocity of viscous vortex rings. *Stud. Appl. Maths* **49** (4), 371–380.
- SCHILLER, L. & NAUMANN, A. 1935 A drag coefficient correlation. *Z. Verein. Deutsch. Ing.* **77**, 318–320.
- VAN SEBILLE, E. *et al.* 2020 The physical oceanography of the transport of floating marine debris. *Environ. Res. Lett.* **15** (2), 023003.
- SENGUPTA, A., CARRARA, F. & STOCKER, R. 2017 Phytoplankton can actively diversify their migration strategy in response to turbulent cues. *Nature* **543**, 555–558.
- SULLIVAN, I.S., NIEMELA, J.J., HERSHBERGER, R.E., BOLSTER, D. & DONNELLY, R.J. 2008 Dynamics of thin vortex rings. *J. Fluid Mech.* **609**, 319–347.
- TINAIKAR, A., ADVAITH, S. & BASU, S. 2018 Understanding evolution of vortex rings in viscous fluids. *J. Fluid Mech.* **836**, 873–909.
- WIDNALL, S. & SULLIVAN, J. 1973 On the stability of vortex rings. *Proc. R. Soc. A: Math. Phys. Engng Sci.* **332**, 335–353.
- ZHOU, W. & DUŠEK, J. 2015 Chaotic states and order in the chaos of the paths of freely falling and ascending spheres. *Intl J. Multiphase Flow* **75**, 205–223.
- ZIMMERMANN, R., GASTEUIL, Y., BOURGOIN, M., VOLK, R., PUMIR, A. & PINTON, J.-F. 2011 Rotational intermittency and turbulence induced lift experienced by large particles in a turbulent flow. *Phys. Rev. Lett.* **106**, 154501.